TAMPEREEN TEKNILLINEN YLIOPISTO
TAMPERE UNIVERSITY OF TECHNOLOGY
Julkaisu 632 • Publication 632

Antti Niemistö

Quantitative Image Analysis Methods for Applications in Biomedical Microscopy

Tampere 2006

Tampereen teknillinen yliopisto. Julkaisu 632
Tampere University of Technology. Publication 632

Antti Niemistö

Quantitative Image Analysis Methods for Applications in Biomedical Microscopy

Thesis for the degree of Doctor of Technology to be presented with due permission for public examination and criticism in Tietotalo Building, Auditorium TB109, at Tampere University of Technology, on the 24th of November 2006, at 12 noon.

Tampereen teknillinen yliopisto - Tampere University of Technology
Tampere 2006

ISBN 952-15-1673-9 (printed)
ISBN 952-15-1718-2 (PDF)
ISSN 1459-2045

Abstract

This thesis describes a systematic procedure for performing quantitative analysis of biomedical microscopy images. The procedure is investigated with four case studies. The goal of the thesis is to illustrate the possibilities of automated image analysis in biomedical microscopy in general and to provide solutions for specific cases. The image analysis methods as well as the biological background of the case studies are presented in such a way that the thesis is accessible for researchers with a background in biology or in engineering.

Quantitative information on biomedical samples has been traditionally obtained by visual inspection of the sample under the microscope. However, manual analysis is subjective, labor-intensive, and slow. All these problems can be overcome by developing automated image analysis methods. The presented procedure has six steps: sample preparation and image acquisition, image pre-processing, image segmentation, feature extraction, validation, and data analysis. The main emphasis of the thesis is in the three steps following sample preparation and image acquisition. They form the core of the procedure: we start with an image, essentially a matrix of real or integer values, and end up with a description of the image at a higher level of abstraction. A simple example would be the extraction of the number of cells in an image. Cell-specific spatial, spectral, and temporal features may be extracted as well. Validation of the obtained results and of the methods used is also very important. In the example given above, we want to be sure that the extracted number of cells is correct. The traditional way of validating results has been to compare the obtained results with results obtained by manual inspection of the cells under the microscope. The thesis proposes new simulation-based ideas for the validation step. The data analysis step uses the quantitative data obtained in the feature extraction step to obtain biologically relevant results.

The first case study considers quantification of *in vitro* angiogenesis. The aims are two-fold. On the one hand, the developed quantitative image analysis method is used together with discrete growth models to study the global properties of angiogenesis. On the other hand, the method is used to study the effects of different agents on *in vitro* angiogenesis. The obtained information can be used in drug discovery, because one of the strategies for treating cancer is to inhibit angiogenesis. In the second case study the motivation is similar: a method for quantifying the effects of different agents on the invasive capability of cancer cells in an *in vitro* invasion assay is presented.

The third case study considers quantification of budding yeast. There are two aims in this case study. The first aim is to obtain information on the cell cycle phase of the population by quantifying bud sizes. The second aim is to study peroxisome biogenesis in budding yeast. In the fourth case study an image analysis method is developed for quantifying lymph nodes in surgical specimens of colorectal cancer. A correlation between patient survival and the size and number of lymph nodes is found.

Preface

The research reported in this thesis was carried out during the years 2002–2006 at the Institute of Signal Processing of the Department of Information Technology at Tampere University of Technology and at the Cancer Genomics Core Laboratory of the Department of Pathology at The University of Texas M. D. Anderson Cancer Center in Houston, Texas, USA.

My sincerest gratitude is due to my supervisor, Professor Olli Yli-Harja, for providing the possibility of working on this subject. His continuous encouragement and support have inspired me along the way.

Without any doubt, Professor Ilya Shmulevich has had the greatest impact on my research, and I am especially grateful to him for his vision, guidance, and friendship. I also acknowledge gratefully my indebtedness to Professor Wei Zhang for providing the possibility of working at his laboratory at The University of Texas M. D. Anderson Cancer Center.

I also owe a debt of thanks to all of my co-authors for their excellent contribution. The type of interdisciplinary research presented in this thesis would not have been possible without the contributions of co-authors with a background in biology and medicine. I would also like to thank my friends and colleagues at the Institute of Signal Processing for creating an inspiring environment. I am especially grateful to Dr. Heikki Huttunen, Dr. Pertti Koivisto, Dr. Marja-Leena Linne, Dr. Harri Lähdesmäki, Matti Nykter, M.Sc., Tommi Aho, M.Sc., Jyrki Selinummi, M.Sc., Pekka Ruusuvuori, M.Sc., Antti Lehmussola, M.Sc., Miika Ahdesmäki, M.Sc., and Jenni Seppälä, M.Sc., for stimulating discussions and valuable comments.

The financial support of Tampere Graduate School in Information Science and Engineering (TISE), the Finnish Cultural Foundation, and Emil Aaltosen Säätiö is gratefully acknowledged.

I wish to thank my parents and my big sister Riitta for their support and encouragement. I would also like to thank my friends for being there.

Tampere, November 2006

Antti Niemistö

Contents

List of publications

I A. Niemistö, V. Dunmire, O. Yli-Harja, W. Zhang, and I. Shmulevich, "Robust quantification of *in vitro* angiogenesis through image analysis," *IEEE Transactions on Medical Imaging*, vol. 24, no. 4, pp. 549–553, April 2005.

II A. Niemistö, V. Dunmire, O. Yli-Harja, W. Zhang, and I. Shmulevich, "Analysis of angiogenesis using *in vitro* experiments and stochastic growth models," *Physical Review E*, vol. 72, no. 6, 062902(1–4), December 2005.

III A. Niemistö, L. Hu, O. Yli-Harja, W. Zhang, and I. Shmulevich, "Quantification of *in vitro* cell invasion through image analysis," in *Proceedings of the 26th Annual International Conference of the IEEE Engineering in Medicine and Biology Society (EMBC'04)*, San Francisco, California, USA, September 1–5, 2004, pp. 1703–1706.

IV A. Niemistö, T. Aho, H. Thesleff, M. Tiainen, K. Marjanen, M.-L. Linne, and O. Yli-Harja, "Estimation of population effects in synchronized budding yeast experiments," in *Image Processing: Algorithms and Systems II*, E. R. Dougherty, J. Astola, and K. Egiazarian, Eds. Proceedings of SPIE, vol. 5014, May 2003, pp. 448–459.

V A. Niemistö, J. Selinummi, R. Saleem, I. Shmulevich, J. Aitchison, and O. Yli-Harja, "Extraction of the number of peroxisomes in yeast cells by automated image analysis," in *Proceedings of the 28th Annual International Conference of the IEEE Engineering in Medicine and Biology Society (EMBC'06)*, New York, USA, August 30 – September 3, 2006, pp. 2353–2356.

VI A. Niemistö, I. Shmulevich, O. Yli-Harja, L. Chirieac, S. R. Hamilton, "Automated Quantification of Lymph Node Size and Number in Surgical Specimens of Stage II Colorectal Cancer," in *Proceedings of the 27th Annual International Conference of the IEEE Engineering in Medicine and Biology Society (EMBC'05)*, Shanghai, China, September 1–4, 2005, pp. 6313-6316.

VII A. Niemistö, I. Shmulevich, V. Lukin, A. Dolia, and O. Yli-Harja, "Correction of misclassifications using a proximity-based estimation method," *EURASIP Journal on Applied Signal Processing*, vol. 2004, no. 8, pp. 1142–1155, August 2004.

Chapter 1

Introduction

The cell is the basic structural and functional unit of all living organisms. All cells have a membrane which separates its interior from its environment and controls what moves in and out. The inside of the membrane consists mostly of a salty cytoplasm. All cells also possess DNA, the hereditary material of genes, and RNA, containing the information necessary to build various proteins. They also contain organelles that have specific functions. The most important organelle of an eukaryotic cells is the nucleus, which is the place where almost all DNA replication and RNA synthesis occur.

The typical diameter of a cell ranges from 1 μm to 100 μm. A microscope is therefore needed for the observation of most cells. The observation can be done through the eyepiece of the microscope or images can be obtained with a camera. The availability of inexpensive digital cameras has enabled new kinds of studies in which a large number of biological samples are analyzed based on digital images. In particular, the structure and functionality of the cell are being studied. The acquired knowledge can be applied in, for example, cancer research and drug discovery.

Traditionally biological samples have been analyzed manually by visual inspection under the microscope. For example, a simple task could be to count the number of cells in a cell population. Analysis performed in this way is naturally very labor-intensive, tedious, and slow, which restricts the number of samples that can be analyzed. This is a serious problem especially when a large amount of data is produced with emerging high-throughput techniques such as cell microarrays [101,110]. The next step has been a move to image-aided or semi-automatic analysis. For example, there are software tools that can be used for counting the number of cells in such a way that the user clicks on the cells with a mouse, and the program automatically counts the number of clicks. Cells that have been already counted can be marked automatically on the image so as to avoid counting a cell twice. Similarly, the area of cells or other features can be measured semi-automatically by drawing the outline of the feature.

Semi-automated tools can provide significant improvements over manual methods in terms of speed and accuracy, but they do not utilize the full potential of image analysis. In particular, if these tools are used by different persons, the results may be differ-

ent for the same image data. This is known as inter-observer variability. Intra-observer variability can also be observed, that is, when the same person performs the analysis twice, the results may differ. Inter- and intra-observer variability are of course present also when the analysis is done by mere visual inspection through the eyepiece of the microscope. The effects have been analyzed quantitatively in [100].

The flow cytometer is another tool for analysis of cells. Measurements are made on fluorescently labeled cells flowing in a solution past a laser beam with detectors measuring fluorescence and light scatter [66]. Flow cytometry is in wide usage, and it is a reliable and reproducible way of obtaining quantitative information on cells. However, the method has its limitations. Most significantly, in flow cytometry the cells must almost always be removed from their natural environment and put into a suspension. This can have significant effects on the behavior of the cells and also makes it impossible to study inter-cellular phenomena. It is also not possible to study subcellular structures.

Automated image analysis has the potential of overcoming the drawbacks of all of the above mentioned analysis methods. A fully automated method does not require any user intervention, which guarantees that there is no inter- or intra-observer variability in the obtained results. More specifically, the same criteria and algorithms are always used in detecting and quantifying the desired features from the images, and the analysis is always performed objectively. Since the analysis can always be performed in exactly the same way, results obtained with automated image analysis are also reproducible. These properties are very important when comparisons are made between samples.

The most crucial step in image analysis is the segmentation of the foreground from the background. Although segmentation has been studied intensely over the past few decades, a single general purpose method does not exist. For each application one needs to find a suitable method from a large pool of available methods. It is typical that none of the standard methods works as such, and it is therefore crucial to understand the most important principles underlying the available methods so that a method that works well can be developed. Some of the most important factors that make segmentation difficult include nonuniform intensity of the background, intensity variations within foreground objects, and clustering of foreground objects. The background variations make it difficult to distinguish the foreground from the background. The intensity variations within the foreground causes over-segmentation, that is, foreground objects split into several objects. On the other hand, clustering of the foreground objects may lead to under-segmentation, that is, several clustered objects are detected as a single object.

Although the solution to an image analysis problem depends heavily on the nature of the image data, the general image analysis procedure is usually the same. The procedure for biomedical microscopy images is described in Chapter 2. The most important image analysis methods are also described. The contributions of the enclosed publications are discussed in Chapter 3. Chapter 4 contains a discussion on some of the present challenges and future directions within the field of biomedical microscopy

imaging and automated image analysis. Chapter 5 concludes the thesis with comments on the enclosed publications.

Chapter 2

Quantitative image analysis

A digital image is a sampled and quantized representation of a continuous image. Let us give a precise definition.

Definition 2.1 A d-dimensional digital gray level image is a mapping of a subset $\mathcal{D}_f$ of $\mathbb{Z}^d$ into a bounded set of nonnegative integers $\mathbb{N}$ given by

$$f : \mathcal{D}_f \subset \mathbb{Z}^d \longrightarrow \{0, 1, \ldots, L\},$$

where L is the maximum gray level (intensity) value.

The notation $f(\mathbf{x})$, $\mathbf{x} \in \mathbb{Z}^d$ is used for the gray level value of a d-dimensional image f at $\mathbf{x}$. In the special case $d = 2$, the notation $f(m, n)$, $m, n \in \mathbb{Z}$ can also be used. In that case the elements of f at a location $\mathbf{x} = (m, n)$ are commonly referred to as pixels. Usually the gray level values are coded using b bits, in which case $L = 2^b - 1$. The values of f are restricted to nonnegative integer values for practical reasons. However, all of the methods presented in this thesis extend directly to images with real-valued pixels.

A binary image is a digital image that has only two possible pixel values.

Definition 2.2 A d-dimensional binary image is a mapping of a subset $\mathcal{D}_f$ of $\mathbb{Z}^d$ into the couple $\{0, 1\}$ given by

$$f : \mathcal{D}_b \subset \mathbb{Z}^d \longrightarrow \{0, 1\}.$$

Definition 2.3 The complement of an image f is given by

$$f^c(\mathbf{x}) = L - f(\mathbf{x}),$$

where L is the maximum intensity value. For binary images $L = 1$.

Gray level and binary images are monochannel images. A multichannel image consists of an array of monochannel images.

Definition 2.4 A multichannel image with c channels is an array

$$[f_1, f_2, \ldots, f_c],$$

where each monochannel image f_i is defined over a common definition domain $\mathcal{D}_f$, see Definition 2.1.

Definition 2.4 means that a vector in $\mathbb{N}^c$ is defined for each pixel of an image with c channels. For example, color images in the RGB color space are multichannel images containing three channels, one for each of the primary colors red, green, and blue.

Digital image analysis refers to the extraction of information from digital images. Often the extracted information is quantitative. For example, one can extract the number of cells in an image. The information can also be qualitative or class information, such as the type of cells in the image. In both cases the aim of image analysis is to describe the contents of the image in some useful way. The images under analysis often contain objects on a background, and then usually the aim is to extract some specific information on the objects. The objects can also be referred to as the foreground. The extracted information can include such features as size, area, shape, brightness, color, and so on.

Quantitative analysis of biomedical microscopy images can be divided into six fundamental steps:

1. Sample preparation and image acquisition
2. Pre-processing of the acquired images
3. Segmentation of the pre-processed images
4. Feature extraction based on the segmented images
5. Validation of the feature extraction results
6. Data analysis based on the extracted features

This chapter covers the most fundamental principles and methods that are applied in these steps. The emphasis is on image processing and analysis methods, and other topics are covered more briefly. Since the intended audience of this thesis includes biologists, the intention is to give an accessible overview of the possibilities and limitations of image analysis.

Textbooks on molecular cell biology, such as the books by Alberts *et al.* [1] and Lodish *et al.* [66], can be used as reference material for many of the topics covered in Section 2.1. Textbooks on digital image processing, such as the books by Gonzalez and Woods [41] and Russ [82], can be used as reference material for topics covered in Sections 2.2 through 2.4. Textbooks on pattern classification, such as the book by Duda *et al.* [30], can be used as reference material for the topics covered in Sections 2.4 through 2.6.

2.1 Sample preparation and image acquisition

Preparation of biological samples and image acquisition should be done carefully so that high-quality images are obtained. Although problems in the image quality can be mitigated in the image pre-processing step or by using robust segmentation methods, one cannot expect to obtain accurate results unless the quality of the images is sufficient. Possible staining of the samples, the choice of the type of microscope and its settings, and the choice of camera and its settings are all important considerations.

Many of the studies with biomedical images are comparative studies. For example, the aim may be to compare the effects of specific agents or treatments on some specific properties of the cells or cell population under study. It is therefore important that the samples have been prepared consistently following exactly the same protocol. It is also important to design the experiment so that appropriate control or reference images will be acquired. These control images may include experiments with no treatment or with treatments whose effects on the features of the cells that are being quantified are known. The purpose of the control images is to enable one to make conclusions on how significant the effects of the other treatments are. As another example, in many studies mutant strains are compared with a reference wild type strain.

In principle it is impossible to study a real world system without interfering with the system itself. With cells and other biological systems the interference is often very significant. For example, instead of studying cells *in vivo* in their natural environment, cells are often studied *in vitro*, that is, they can be cultured in a solution of nutrients in a plastic dish or specific *in vitro* assays may be used. Cells or tissue may also be removed from their natural information and fixed (killed) before being studied. It is very important to understand how the experiment was made so that one is able to make the right conclusions regarding cells (or tissue) that are in their natural environment.

2.1.1 Staining

In many experiments the cells or the tissue absorb about the same amount of visible light as the medium of the sample. The contrast obtained with a light microscope is therefore usually insufficient for image analysis. More informally we can say that most cells are colorless and translucent. In fact, many cells are more than 50 per cent water by weight. One way of improving the contrast is to stain the cells.

Many chemical stains have an affinity for molecules that have specific features. For example, hematoxylin and eosin stains can be used in many applications. Hematoxylin has an affinity for basic amino acids on many proteins and eosin has an affinity for acidic molecules. The different affinity properties mean that these dyes stain various cell types sufficiently differently that they are distinguishable visually. Numerous chemical staining protocols are available for specific applications. For example, the hematoxylin and eosin stain is commonly used for staining histological sections of many types of tissue.

Fluorescent staining provides an extremely versatile and powerful way of visualizing cells and subcellular structures by microscopy. Fluorescent markers that bind to specific protein structures are used. They absorb light at one wavelength and emit light at another longer wavelength. When a fluorescent molecule absorbs a photon, it is left in an excited state, that is, the energy of the molecule is increased by the energy of the photon

$$\Delta E = \frac{hc}{\lambda}, \tag{2.1}$$

where h is Planc's constant, c is the speed of light, and λ is the wavelength of the electromagnetic wave. Some of the absorbed energy is dissipated as heat and the rest is emitted as light having a longer wavelength than the absorbed light. This phenomenon is known as the Stokes shift. It enables the separation of the absorbed and emitted light by optical filters, allowing visualization of the cells or subcellular structures stained by the fluorescent marker.

2.1.2 Microscopy

The microscope is an essential tool for many biologists. The obvious reason for this is that the size of most cells is below the upper limit of the resolution of the human eye. The basic ideas of magnification using lenses were already known in ancient times, and the development of the modern microscope can be regarded to have started with the work of Zacharias and Hans Janssen in the late 16th century.

The most important property of any microscope is its ability to distinguish between two closely positioned objects, that it, its resolution. The resolution of a light microscope is given by [66]

$$d = \frac{0.61\lambda}{N\sin(x)}, \tag{2.2}$$

where λ is the wavelength of the incident light, N is the refractive index of the medium between the sample and the objective lens, and x is the angular aperture. The angular aperture can be defined as the half-angle of the cone of light entering the objective lens from the sample, see Figure 2.1.

The maximum angular aperture for the best objective lenses is 70°. The refractive index for air is by definition equal to unity. Higher values of up to $N = 1.5$ can be obtained with an immersion oil. If we further assume visible light of shortest wavelength, $\lambda = 450$ nm (blue), we obtain the value $d \approx 195$ nm. This is considered as the limit of resolution of light microscopes, which means that only objects with a diameter 195 nm or more can be detected with a light microscope. Note that the magnification of the microscope is not part of Equation (2.2). It is in fact important to realize that merely enlarging the image does not result in a capability to distinguish small details. If a higher resolution is required, electron microscopy can be used in certain applications to obtain resolutions of up to 0.1 nm.

Several optical configurations for light microscopes exist, see, for example, [94]. In the common bright field configuration, light that is not absorbed by the sample creates

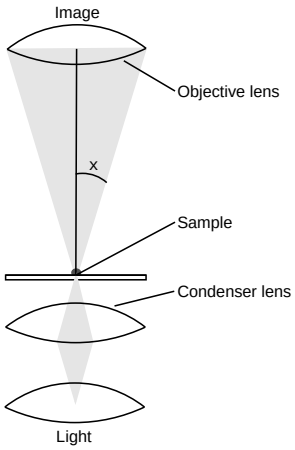

Figure 2.1: The optical pathway of a light microscope from the light source to the objective lens.

the image. If the sample has not been stained, the image may have insufficient contrast. The contrast can be enhanced by techniques that make use of differences in the refractive index of cell structures. In dark field microscopy this is achieved by making the main field of observation dark by placing a disk on the condenser. Light enters the sample from an oblique angle and the image is created by light that is scattered by the sample. The sample is thus viewed in front of a dark background. For an illustration of these principles, see Figure 2.2. The phase contrast microscope generates an image in which the brightness of a region of the sample depends on the refractive index of that region. Images with a high contrast can be obtained for thin samples using this technique. The differential (Nomarski) interference microscope uses a similar principle: the brightness of the obtained image depends on changes in the refractive index and thickness of the sample.

The two-dimensional image obtained with the bright field microscope consists of a superposition of in-focus and out-of-focus regions of the sample. It is therefore not suitable for imaging thick samples. Also, in the case of a sample of cells growing loose in a solution it may not be possible to get all the cells in focus. The confocal microscope avoids this problem by permitting visualization of each focal plane separately. The basic principle is that the sample is illuminated one point at a time, and the detector only registers light emitted from the illuminated point. Three dimensional images can be obtained by combining images taken at different focal planes.

Fluorescently stained samples are detected with a fluorescence microscope. This is similar to light microscopy. The difference is that the illuminating light is passed through two sets of filters. The first filter ensures that only the absorption wavelengths of the fluorescent marker hit the sample. The second filter blocks the absorption wavelengths and passes to the detector only those wavelengths that are emitted as the marker fluoresces.

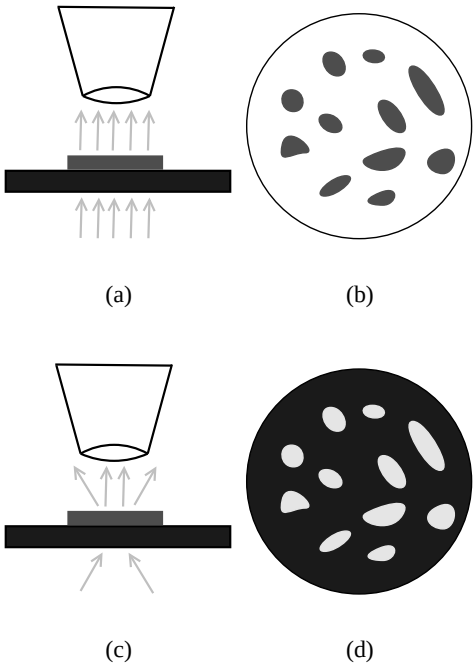

Figure 2.2: In bright field microscopy, (a) the image is created by light that is not absorbed by the sample, and (b) cells are seen as dark objects on a bright background. In dark field microscopy, (c) the image is created by light that is scattered by the sample, and (d) cells are seen as bright objects on a dark background.

2.1.3 Imaging

Imaging is performed with a digital camera attached to the microscope. The camera may be attached to the eyepiece or to the trinocular port of the microscope. There are also microscopes with a built-in digital camera. In recent years the quality of inexpensive digital cameras has increased rapidly, making the quality of the camera typically not a key factor in determining the quality of the microscopy images. Color images should be taken only if there is useful color information in the samples. Most color cameras produce RGB images, which are three-channel images of the form $[r, g, b]$. The channels r, g, and b define an additive mixture of the three primary colors red, green, and blue.

Imaging should always be done consistently with the same microscope and camera settings for all samples. All features that automatically select the settings of the microscope or the camera should be disabled, because in that case it is impossible to verify that the same settings have been used for all images, rendering accurate comparisons impossible. Ideally one should get the raw image data straight from the sensor of the camera. However, in practice a sufficient quality can also be obtained by saving

the images in a standard image format that does not use lossy compression. All other automated processing within the camera or the imaging software should be disabled, because the automated processing methods are usually proprietary to the camera or software manufacturer. Proprietary methods make it impossible to know what processing has been made with the data, making it impossible to know afterwards if a given feature in the obtained image is a processing artefact or something that is really part of the biological sample.

Many systems have a gain setting that can be used to amplify the signal obtained from the camera. This naturally also amplifies the noise in the signal. Therefore care should be taken in using the gain setting so that the amplified noise does not result in deterioration of the image quality. For this reason it is usually better to increase the intensity of the illumination than to adjust the gain, and a good balance should be found between these settings. One should also be careful in using these setting so as not to get over-exposed images, in which some of the pixel values have been clipped to the maximum value. Especially if the intensities of the stained cells or subcellular structures are compared, it is important that the illumination and gain settings are the same for each image. Many microscopes have features that allow automated selection of the best illumination settings for the sample under the microscope, and such features should naturally be disabled if intensities are compared. Finally, since the samples are three-dimensional, special care should be taken in finding the correct focus. Poor focus results in blurred images, for which it is difficult to perform quantitative image analysis accurately.

2.2 Pre-processing

Pre-processing refers to processing steps that need to be taken to make the acquired image suitable for quantitative analysis. The aim is to reduce the effects of imperfect image acquisition. The priority should always be to acquire the best quality images possible in the image acquisition step. However, some pre-processing steps are usually nevertheless needed, no matter how image acquisition is performed. Moreover, in practice it may be the case that not enough attention is payed to image quality in image acquisition. If this is realized too late, it may be impossible to perform imaging anew. For example, the intensity of the stains in the samples may have become too weak.

Many of the methods that are used are image enhancement or restoration methods. The specific steps that need to be taken and the methods that are used depend on the subsequent analysis methods.

2.2.1 Color space conversions

Digital color images are usually stored in the RGB color space. The RGB color space is also the color space used by most digital cameras. However, because the RGB color

space is in many cases not useful in digital image processing, a conversion to another color space is a typical pre-processing step.

If the color image does not include any significant or useful color information, retaining the luminance information and discarding the chrominance (color) information is the best approach. This is commonly done by [52]

$$f(\mathbf{x}) = 0.2989r(\mathbf{x}) + 0.5870g(\mathbf{x}) + 0.1140b(\mathbf{x}), \tag{2.3}$$

where r, g, and b are the RGB components of the image. Because of the properties of the human eye, the green channel is the dominant channel in the conversion. In fact, instead of the conversion (2.3), the green channel can be used as a luminance image.

If there is significant color information in the image, a perceptually uniform color space should be used. In a perceptually uniform color space the metric distance between two colors is proportional to the human perception of color differences. This is important, because many image analysis methods use color differences as measured by a metric in the color space. The CIE L*a*b* color space defined by the *Commission Internationale l'Éclairage* (CIE) is usually used [24]. In this color space the L component represents the luminance of the color, the a component represents its position between magenta and green, and the b component represents its position between yellow and blue. Some image processing methods may require gray level images, and these methods can be applied to the L component. The conversion from the RGB color space to the CIE L*a*b* color space is done by assuming the sRGB color space [4]. The conversion is based on an intermediate system known as the CIE XYZ, which is derived from sRGB by [106]

$$\begin{aligned} X(\mathbf{x}) &= 0.4124r(\mathbf{x}) + 0.3576g(\mathbf{x}) + 0.1805b(\mathbf{x}), \\ Y(\mathbf{x}) &= 0.2126r(\mathbf{x}) + 0.7152g(\mathbf{x}) + 0.0722b(\mathbf{x}), \\ Z(\mathbf{x}) &= 0.0193r(\mathbf{x}) + 0.1192g(\mathbf{x}) + 0.9505b(\mathbf{x}), \end{aligned} \tag{2.4}$$

where r, g, and b are the sRGB components of the image. The components of the CIE L*a*b* color space are then obtained by

$$\begin{aligned} L(\mathbf{x}) &= 116F(Y(\mathbf{x})/Y_n) - 16, \\ a(\mathbf{x}) &= 500[F(X(\mathbf{x})/X_n) - F(Y(\mathbf{x})/Y_n)], \\ b(\mathbf{x}) &= 200[F(Y(\mathbf{x})/Y_n) - F(Z(\mathbf{x})/Z_n)], \end{aligned} \tag{2.5}$$

where

$$F(t) = \begin{cases} t^{1/3} & \text{if } t > 0.008856, \\ 7.787t + 16/116 & \text{otherwise}, \end{cases} \tag{2.6}$$

and X_n, Y_n, and Z_n represent a reference white. The CIE standard illuminant D_{65} yields $X_n = 0.3127$, $Y_n = 0.3290$, and $Z_n = 0.3583$.

2.2.2 Correction of nonuniform illumination

When the microscope is set up properly, a roughly uniform illumination of the sample can be achieved. However, in practice the illumination pattern is seldom perfectly uniform in microscopy images. The nonuniformity may be caused by a number of factors. These include imperfections of the illumination filament and of the design of the light path between the camera and the microscope. The behavior of the camera itself may also be behind the nonuniformity, especially if a camera that has not been designed for microscopy is used. For example, the lens of the camera may show vignetting, that is, reduction in image brightness in the image periphery compared to the image center [61].

Correction of nonuniform illumination is therefore an important pre-processing step. Its role is in fact crucial when microscopy images are used to compare intensity measures from different parts of a sample. Moreover, many image analysis methods rely on the assumption that the same type of object will have the same intensity irrespective of its spatial location. Global thresholding is a simple example of such a method. Sometimes the problem of nonuniform illumination is circumvented by cropping from the image a region of interest whose background is uniform enough. However, this approach has the severe disadvantage that typically a substantial percentage of the image data is lost.

The relation between the acquired two-dimensional nonuniformly illuminated image f and its corresponding uniformly illuminated image u can be described by the linear model

$$f(\mathbf{x}) = u(\mathbf{x})\xi_m(\mathbf{x}) + \xi_a(\mathbf{x}), \tag{2.7}$$

where ξ_m and ξ_a are the multiplicative and additive nonuniformity components, respectively [98]. If the nonuniformity components ξ_m and ξ_a are known, correction of nonuniform illumination is achieved by inverting the linear model by

$$\hat{u}(\mathbf{x}) = \frac{f(\mathbf{x}) - \xi_a(\mathbf{x})}{\xi_m(\mathbf{x})}. \tag{2.8}$$

The correction problem can be simplified by assuming that only one of the nonuniformity components is involved in the corruption of the image u. Then, the corrected image $\hat{u}$ can be obtained by either

$$\hat{u}(\mathbf{x}) = f(\mathbf{x}) - \xi_a(\mathbf{x}) + C_a \tag{2.9}$$

or

$$\hat{u}(\mathbf{x}) = \frac{f(\mathbf{x})}{\xi_m(\mathbf{x})} C_m, \tag{2.10}$$

where $C_a \in \mathbb{R}$ and $C_m \in \mathbb{R}$ are normalization coefficients needed to restore the desired average grey level. Whether the additive or the multiplicative model should be used depends on the characteristics of the camera. The additive model is correct if the sensor response function is logarithmic, while the multiplicative model is correct for

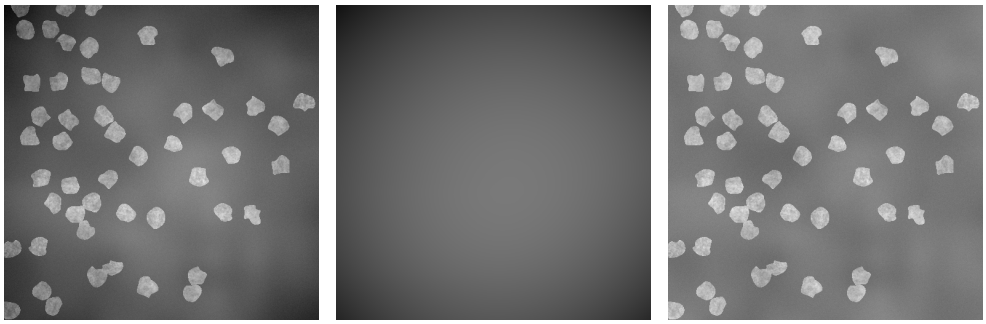

(a) (b) (c)

Figure 2.3: (a) A simulated image of a cell population with nonuniform illumination. (b) The nonuniform illumination estimated as a polynomial surface. (c) The original image after correction of nonuniform illumination by Equation (2.9) with C_a equal to the maximum value of the estimate ξ_a.

a linear device [82]. Figure 2.3 shows an example of correcting nonuniform illumination under the assumption of the additive model and C_a equal to the maximum value of the nonuniformity estimate ξ_a. The original image was obtained with the simulator described in [60].

In the process of subtracting an image from another or dividing an image by another, the dynamic range of the pixel values is reduced. The greater the variation in the intensity of the background image, the greater the reduction in the dynamic range. Therefore, one should not merely rely on digital correction of illumination uniformities. Rather, one should ideally put the emphasis on designing the illumination system so that it produces as uniform an illumination as possible.

The nonuniformity components ξ_a and ξ_m can be obtained at the imaging step by acquisition of additional calibration images. For example, they can be obtained by imaging an empty or defocused field [98]. However, the use of calibration images is not always feasible. For example, at the imaging step it may not be known that automated image analysis is later going to be performed on the images, and thus the need for calibration images is not known before it is too late to obtain them. It can also be difficult to notice a small nonuniformity of the illumination at the imaging step, and thus the need for calibration images may be overlooked at that point.

Instead of using calibration images for estimating the nonuniformity components, one can estimate the nonuniformity components from the acquired image. This is often referred to as the data-driven approach. It is clear that from a practical viewpoint the data-driven approach is simpler than using calibration images. There are several standard approaches to the estimation problem. Let us now briefly review the three main categories: low-pass filtering, morphological filtering, and fitting a nonunifor-

mity model. Usually one can assume a purely additive or a purely multiplicative model and use either Equation (2.9) or Equation (2.10).

The low-pass filtering approach is based on the assumption that the background variation due to nonuniform illumination is a low frequency signal that can be separated from the higher frequencies of the objects. This can be done in the frequency domain by using the discrete Fourier transform [82] or one can use frequency selective filters in the spatial domain. A method for estimating the nonuniformity component by filtering the nonuniformly illuminated image with a Gaussian filter was proposed in [61]. The disadvantage of the low-pass filtering methods is that the appropriate cut-off frequency depends on the image. Also, the basic assumption that the nonuniformity component and the underlying image are separable in the frequency domain is usually not true.

If the objects of interest are small compared with the scale of background variations and the background is either everywhere darker or everywhere lighter than the objects, the background can be estimated using the basic morphological operations. Both requirements are often met in microscopy imaging. For the case of light objects on a dark background, Russ [82] proposes to use the morphological erosion as the background estimate and Soille [93] proposes to use the morphological opening (erosion followed by dilation). For the opposite case, they propose the morphological dilation and closing (dilation followed by erosion), respectively. Since erosion and dilation are essentially local minimum and maximum operations, respectively, they are able to filter out light and dark objects. The size of the local neighborhood depends on the size and shape of the objects: it must be large enough so that at each pixel it contains at least one background pixel.

The nonuniformity component can also be estimated by approximating the image background by a smoothly varying function. This approach is often referred to as surface fitting or fitting a background function. The approach can be employed if the illumination nonuniformity follows a simple pattern, which often is the case in microscopy. A popular choice for the estimate of ξ_a or ξ_m is to use a polynomial surface [98]. In this class, the second-order polynomial surface is often the most appropriate choice. Another popular choice for the estimate is to use B-splines [64]. This choice has the advantage that B-splines are by definition continuous in the second derivative and therefore always smooth. Moreover, as with polynomials, the ability to vary the number of control points gives flexibility. In both cases the problem can be posed as a least squares problem and is therefore efficient to solve.

2.2.3 Noise reduction

There are many noise sources in microscopy imaging, the most significant ones being photon noise, thermal noise, readout noise, and quantization noise [99]. The two first noise sources have a Poisson distribution, readout noise is Gaussian, and quantization noise is uniformly distributed. Only the last two noise sources are additive and independent of the image.

The noise from the above mentioned sources should generally be suppressed by restoration methods that take into account the distribution and other properties of the noise components. However, in practice the noise intensity is usually negligible in microscopy imaging, and noise reduction may not be necessary at all. Further, low intensity noise can often be removed by simple filtering techniques, for example using the Gaussian low-pass filter or the median filter [7]. Image averaging [56] is also routinely used, especially in fluorescent microscopy. Although noise suppression by image averaging is based on the assumption of uncorrelated zero mean noise, an assumption that does not hold in microscopy imaging, the method is very useful in practice.

One should always keep in mind that noise removal and detail preservation are conflicting requirements, and an acceptable compromise between the two needs to be found when the image contains noise. Therefore, the emphasis should be in avoiding noise in the image acquisition step. Photon noise is caused by the quantum nature of light and can never be avoided. However, thermal noise from the sensor of the camera can be reduced by cooling the sensor, readout noise is negligible unless one needs to read several images per second, and quantization noise can be made negligible by using at least 8 bits per pixel.

2.2.4 Region of interest selection

Many biological assays contain circular wells, but digital cameras produce rectangular images. One possibility is to acquire an image that contains a rectangular area within the well. This can be thought of as choosing a rectangular region of interest at the image acquisition step. The drawback of this approach is that a substantial part of the well cannot be used in the subsequent image analysis. The alternative approach is to acquire an image that contains the whole well. In that case an appropriate circular region of interest needs to be detected as a pre-processing step. Many of the segmentation methods that are described in Section 2.3 can be used to find a binary mask that defines the region of interest.

There can also be other situations in which region of interest detection is needed. For example, cells localized in the segmentation step may be used as the regions of interest in the detection of subcellular structures.

2.3 Segmentation

Segmentation can be defined as the process by which an image is divided into its constituent objects and the background. It is often the most crucial and the most difficult step in an image analysis task. Segmentation has been studied intensively over the past few decades and numerous segmentation methods have been developed. However, a general solution to the segmentation problem is not available.

In quantitative image analysis of biomedical images one of the frequently extracted image-specific features is the number of foreground objects in the image. The objects

could be, for example, cells of a specific type. This feature can be readily extracted if the objects can be segmented from the image background and each other. However, if the segmentation is not accurate, the extracted number of objects may be false. If one is to extract object-specific spatial, spectral, or temporal features from the images, the requirements for the accuracy of segmentation are even stricter. For example, it is clear that features such as the area of a cell or the intensity of its stain are very sensitive to the accuracy of segmentation. It is thus clear that the success of the final quantitative analysis is dependent on the accuracy of segmentation.

Even though segmentation methods are often very application-specific, there are many general principles that are applied in one way or another in most segmentation methods. Most methods are based on one of two basic properties of intensity values: discontinuity and similarity. Methods based on discontinuity try to find abrupt changes in image intensity, and define the different regions based on these discontinuities. Edge detection by gradient filtering is an example of a method in this category. Methods that are based on similarity partition the image into regions that are similar according to a set of predefined criteria. This category includes such methods as thresholding, clustering, region growing, and region merging and splitting. This section concentrates on similarity-based methods, because in the segmentation of biomedical microscopy images they are usually more useful than discontinuity-based methods.

2.3.1 Thresholding

Due to its simplicity and intuitive properties, thresholding is a central image segmentation method. For bright objects on a dark background it can be defined by

$$f_T(\mathbf{x}) = \begin{cases} 1 & \text{if } f(\mathbf{x}) > T, \\ 0 & \text{if } f(\mathbf{x}) \leq T, \end{cases} \tag{2.11}$$

where $f(\mathbf{x})$ is the gray level of the point $\mathbf{x}$ from the image to be thresholded, $f_T(\mathbf{x})$ is the respective point in the thresholded image, and T is the threshold. A pixel in f_T with the value 1 is called a foreground or object point and a pixel with the value 0 is called a background point. If one has dark objects on a bright background, the roles of 1 and 0 are swapped. If the threshold T is the same for the whole image, the threshold is called global. If a different threshold is used for different parts of the image depending on some local properties, the threshold is called local. It is also possible to replace the image f with an image that has been obtained by replacing the original pixel values with the values of some local property of the pixels. This local property could be, for example, the local average gray level or the local variance.

Research on thresholding has concentrated on automated selection of the optimal threshold T for a given image f. Since the transition between the object and its background is often diffuse, it can be difficult for a human to decide where the object ends and the background begins. The task is even more difficult for a computer: it is difficult to select the optimal threshold automatically. In fact, a satisfactory general solution to

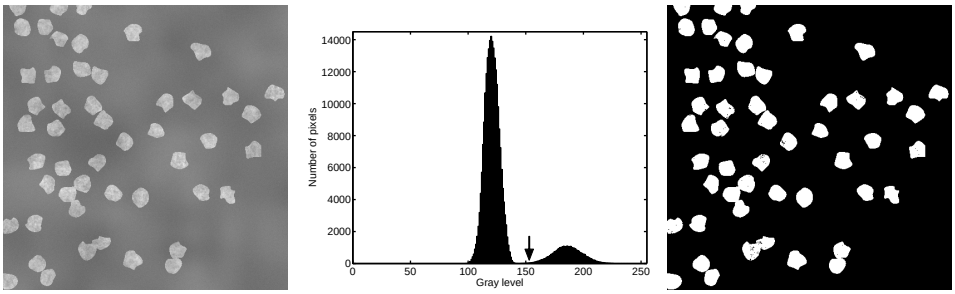

(a) (b) (c)

Figure 2.4: (a) A simulated image of a cell population. (b) The histogram of the simulated image. The arrow points to the threshold $T = 153$ obtained with Otsu's method. (c) The image after thresholding.

the threshold selection problem does not exist. To make matters worse, a small change in the threshold may have a large impact on the subsequent analysis, as the quantification of many features such as the area and the mean pixel intensity of the object are directly dependent on the threshold.

Some of the first papers on automated selection of the threshold were published in the 1960s (see, for example, [29]). An early paper by Prewitt and Mendelsohn [77] also applied thresholding and automated threshold selection to the analysis of cell images. The review papers by Glasbey [39], Sahoo *et al.* [83], Sezgin and Sankur [89], and Sieracki *et al.* [91] give a good overview of the available methods. Probably the most widely used single method is the one by Otsu [75], which selects the threshold in such a way that the between-class variance of the gray levels of the background and objects is maximized, and the intra-class variance is minimized.

In many methods the threshold is selected on the basis of the histogram of the image. If the image has a bimodal histogram, one can often assume that one of the modes represents the background and the other one the foreground, and the threshold should be selected in the valley between the two modes. Otsu's method is a histogram-based method, and can find an appropriate threshold for images with bimodal histograms. An example is shown in Figure 2.4. The image in Figure 2.4(a) is the same as the image in Figure 2.3(c). Otsu's method is useful even if the histogram is not bimodal. An example is shown in Figure 2.5, in which the original image shows *in vitro* angiogenesis.

Thresholding does not have to be the final step in the segmentation procedure. Rather, the thresholding result can be a starting point for further processing. The further processing can consist of operations on the binary image alone, or the binary image can be used together with the original image to refine the segmentation. Sections 2.3.4 to 2.3.6 describe some of these post-processing methods.

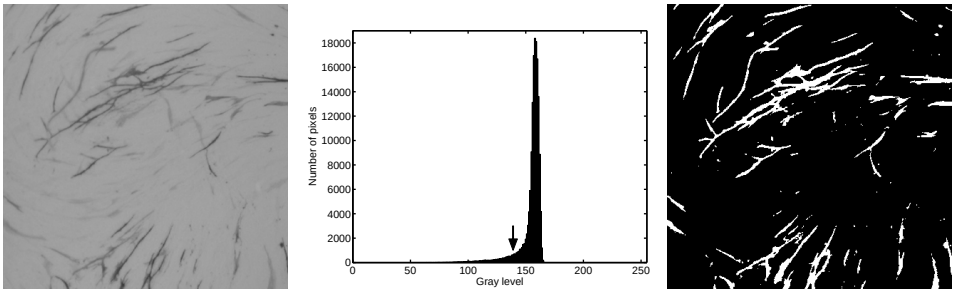

(a) (b) (c)

Figure 2.5: (a) A image of *in vitro* angiogenesis. (b) The histogram of the image. The arrow points to the threshold $T = 139$ obtained with Otsu's method. (c) The image after thresholding.

2.3.2 Clustering

The segmentation problem can be posed as a classification problem. In the simplest case one has two classes, the foreground and the background, but it is also possible to have more classes. For example, there can be several foreground classes that correspond to different types of cells. Supervised classification methods require training images for which the correct classification is known for each pixel. Since this kind of ground truth data is difficult to obtain, unsupervised classification methods, also referred to as clustering methods, are more suitable for segmentation.

Clustering can be defined as the organization of a collection of patterns into clusters based on similarity. Patterns within a valid cluster are more similar to each other than they are to patterns belonging to a different cluster. The patterns are represented by vectors in a feature space. An example of clustering 27 samples into 5 clusters in a two-dimensional feature space is shown in Figure 2.6. Patterns belonging to the same cluster are denoted with the same symbol.

A large number of clustering methods can be found in the literature, including K-means clustering [47, 69], fuzzy C-means clustering [13, 32], and nearest neighbor clustering [67]. An extensive review of clustering methods can be found in [53]. Instead of defining similarity, most clustering methods define the dissimilarity between two patterns by using a distance measure defined on the feature space. Common distance measures in a d dimensional space include the Euclidean distance

$$d_E(\mathbf{a}_i, \mathbf{a}_j) = \left(\sum_{k=1}^{d} (a_{i,k} - a_{j,k})^2 \right)^{1/2} \tag{2.12}$$

as well as the Mahalanobis distance

$$d_M(\mathbf{a}_i, \mathbf{a}_j) = \left((\mathbf{a}_i - \mathbf{a}_j) \Sigma^{-1} (\mathbf{a}_i - \mathbf{a}_j)^{\mathrm{T}} \right)^{1/2}, \tag{2.13}$$

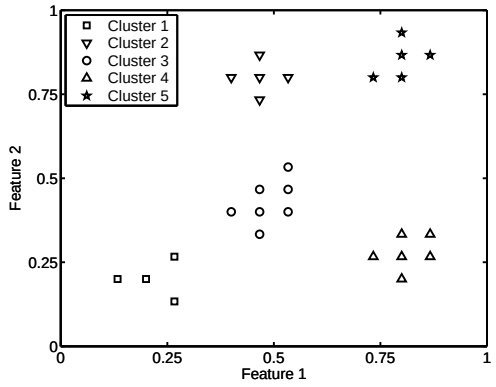

Figure 2.6: Clustering in a two-dimensional feature space.

where $\mathbf{a}_i$ and $\mathbf{a}_j$ are the feature vectors of the patterns i and j, and Σ is the covariance matrix of the distribution from which $\mathbf{a}_i$ and $\mathbf{a}_j$ are taken.

When clustering is applied to image segmentation, a feature vector is defined for each pixel, and the clustering method determines whether the pixel belongs to the background or one of the foreground classes. One of the possible features is the intensity value of the pixel. In fact, thresholding can be thought of as a clustering method that uses the intensity as the only feature. The possibility to use additional features means that clustering is a more flexible segmentation method than thresholding: clustering can be successfully applied in many situations in which thresholding does not give acceptable results. The features used in clustering are usually local features such as the local mean and the local variance. If one has color images and the background and the foreground have different colors, one can use the color components as features. A perceptually uniform color space such as the CIE L*a*b* color space [24] should be used so that the measured dissimilarities are proportional to the human perception of color differences.

Correction of misclassifications

There may be misclassifications in the class data obtained with a classification or clustering method. Specifically, in image segmentation some pixels may get a foreground label even though the background label would be correct, or vice versa. If one has adequate ground truth information that can be used as training data, the misclassification correction method proposed in Publication VII can be used. The method is applied in a sliding window fashion. Suppose that the samples of class data in the sliding window are given by the multiset $B = \{b_1, b_2, \ldots, b_N\}$. Then the output is given by

$$C(B) = \arg\min_{\beta \in B} \sum_{i=1}^{N} w(\beta, b_i), \tag{2.14}$$

where w is a proximity function that defines the interclass distances, and can be obtained by training the method with images for which the ground truth is available.

The successful application of the method requires that the data has several classes. Even if there will ultimately be just two classes, that is, the foreground class and the background class, it is possible to use additional classes in the initial classification. For example, K-means clustering with $K > 2$ can be used for initial classification. The obtained data can then be processed with Equation (2.14) in such a way that the output is always required to be one of two classes.

If ground truth data is not available, the majority filter can be used to correct the most obvious misclassifications [62]. The majority filter is a sliding window filter that chooses as output the class that has most representatives in the window. Weighted majority filters can also be used.

2.3.3 Region growing

Region growing is a general class of segmentation methods that group pixels into larger regions based on predefined similarity criteria. Region growing methods start with a set of seed points. Neighboring points are examined one at a time, and are added to the growing region if they have properties sufficiently similar to the points in the growing region. The procedure continues until no more pixels can be added. The selection of the seed points and the similarity criteria depend on the nature of the problem under consideration. The fundamental similarity criterion is the similarity of the gray levels of the pixels. Local properties of the pixels can also be used as similarity criteria.

The watershed transformation is a popular region growing method that has proved very useful in many areas of image segmentation, including the segmentation of biomedical microscopy images (see, for example, [63, 65, 70, 108]). The method was originally suggested in 1978 by Digabel and Lantuéjoul [27], and extended to a more general framework by Beucher and Lantuéjoul [12]. The basic idea of the watershed transformation is usually described with an analogy to flooding water, hence also the name of the method. The image is thought of as a topographic map, and water is flooded from each regional minimum in such a way that the water rises at a uniform rate. When the rising water from two regional minima is about to merge, a dam (watershed) is built to prevent the merging. The flooding will eventually stop when only the tops of the watersheds are visible above the water line. These watershed lines define the segmentation result. The main difference between the watershed method and ordinary region growing is that the watershed method takes up a new intensity layer in each iteration instead of a new neighbor layer.

The watershed transformation is usually applied to the gradient of the image rather than the image itself. The reason is that the regional minima of the gradient image correlate well with both the foreground objects and the background, whereas the largest values of the gradient image are at the boundaries between the background and the objects. The gradient image is commonly obtained by convolving the image with gradient

operators [36]. There are typically a very large number of regional minima in a gradient image, largely due to noise and other irregularities. Because there is a one-to-one correspondence between the number of regional minima and the number of segmented regions, direct application of the watershed transformation leads to over-segmentation. However, watershed segmentation methods in which over-segmentation can be controlled can be found in basic textbooks on image processing.

Let us look at one of the many watershed segmentation methods in which over-segmentation can be controlled. Instead of letting water flood from all regional minima of the gradient image, the method selects only the deepest regional minima as seeds by using the h-minima transformation [93]. The h-minima transformation suppresses all minima whose depth is less than a given nonnegative threshold level h. A small h results in many seeds, often more than one seed per object, which results in over-segmentation. A large h results in fewer seeds, and some objects may not get a seed at all, which results in under-segmentation. In both cases the segmentation results can be improved by post-processing methods, see Sections 2.3.4 and 2.3.5. It is also possible that over-segmentation and under-segmentation happen simultaneously in different parts of an image.

Figure 2.7 shows an example of watershed segmentation with the method described above. The image in Figure 2.7(a) is the same as the image in Figures 2.3(c) and 2.4(a). Figure 2.7(b) shows the gradient obtained by the Sobel operator. The values of the gradient have been normalized into the interval $[0, 1]$. Figure 2.7(c) shows the watershed segmentation result when the value $h = 0.2$ is used in the h-minima transformation that is applied to the gradient image. The result is similar to the thresholding result presented earlier in Figure 2.4(c). For comparison, the watershed segmentation result for the case of $h = 0.05$ is shown in Figure 2.7(d). Severe over-segmentation is evident.

2.3.4 Region merging

Region merging is often needed as a post-processing step after initial segmentation. The aim is to reconnect regions that belong to the same over-segmented foreground object. A large number of region merging methods have been proposed in the literature. They generally base the merging decision on the similarity of the intensity levels of adjacent objects (see, for example, [46]) or on the gradient at the edge between adjacent objects (see, for example, [108]). The idea is that two adjacent regions are likely to belong to the same object if their average intensity levels are similar or if the gradient of the edge between them is low. The method proposed in [48] combines these two approaches. Additionally, if a minimum area that a correctly segmented object can have is known, an object that is smaller than this minimum should be merged with one of its neighbors. If the object has several neighbors, the properties mentioned above should be compared to select the best neighbor to merge with. In [16] a watershed merging method is proposed. The method can be applied after watershed segmentation. The idea is analogous to letting rain fall over a landscape. The regions defined by the

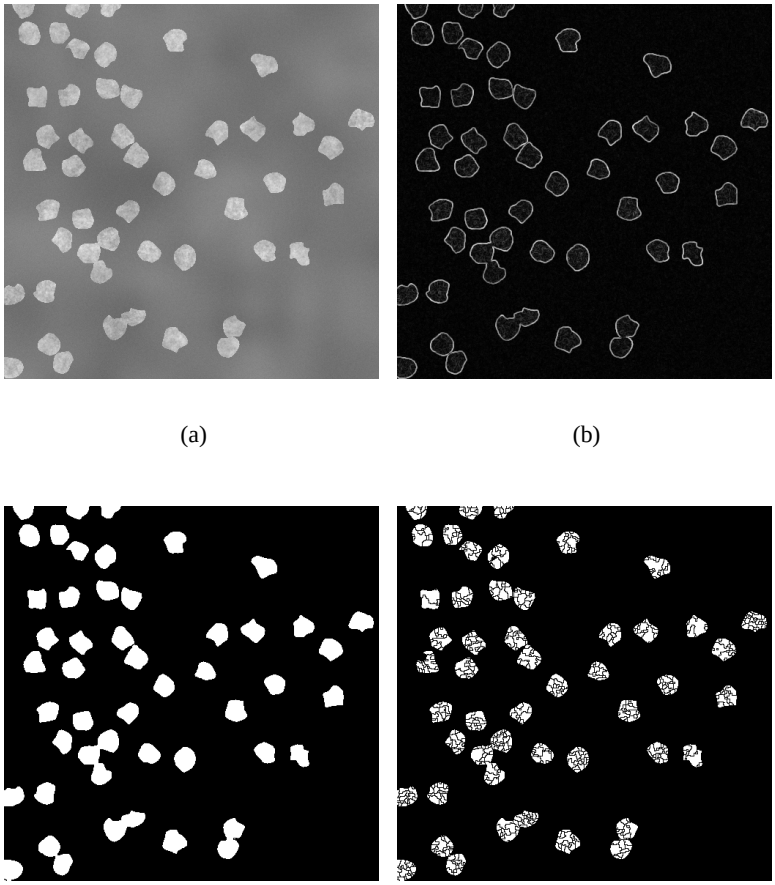

(a) (b)

(c) (d)

Figure 2.7: (a) A simulated image of a cell population. (b) The gradient of the simulated image. (c) A watershed segmentation result with moderate under-segmentation. (d) A watershed segmentation result with severe over-segmentation.

watersheds lines get filled progressively until an overflow to the neighboring region occurs, merging the overflown regions.

2.3.5 Region splitting

Region splitting is often needed as a post-processing step after initial segmentation. Foreground objects that are clustered together are usually not recognized as distinct regions by thresholding and clustering methods, and the same can happen also with region growing methods. The aim of region splitting is to separate under-segmented regions that correspond to two or more different foreground objects.

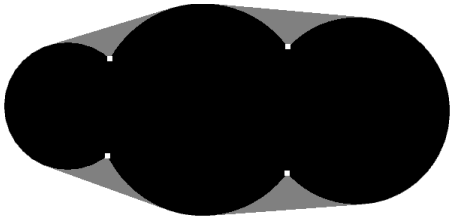

Figure 2.8: A concave region (black), its convex hull (black and gray), and potential splitting points (white).

There are many methods that merely detect regions that correspond to several clustered objects, but do not provide a way to do the actual splitting. A review of some of these detection methods can be found in [11]. The detection is commonly done with a classifier using features that relate to the shape and area of the regions as well as features that relate to the intensity of the regions (see [80] for an extensive list of possible features).

The detection methods can be useful as a first step of a region splitting method. The actual splitting is done as a separate second step for those regions that have been detected as corresponding to several clustered objects. The advantage of this approach is that if the splitting method sometimes splits correctly segmented regions, the first criterion may be used to exclude such regions from splitting. Conversely, some splitting methods may choose not to split a region given as an input if a satisfactory split cannot be found. Because more than two regions may be clustered together, splitting should be applied iteratively until no further splitting is necessary.

Many cell types have approximately convex shapes. Therefore in many applications it can be assumed that under-segmented regions that need to be split are concave, whereas correctly segmented regions are approximately convex. The convex hull is therefore often used to detect splitting points, see, for example, [107]. The convex hull of a concave region is the smallest convex region containing the concave region, see Figure 2.8. Subtracting the concave region from the convex hull gives us the concavity regions (marked gray in Figure 2.8) of the concave region. The deepest point of a concavity is defined as the point that is inside the concavity and whose Euclidean distance to the border of the convex hull is largest. These points (marked with white squares in Figure 2.8) are used as endpoints of splitting lines.

The watershed transformation can also be used to split regions based on their shape [93]. The underlying assumptions on the concavity of under-segmented regions and the convexity of correctly segmented regions are the same as in the method described above. The watershed splitting method has been used for separating clustered cells in, for example, [108].

The watershed splitting method proceeds as follows. First, a distance transformation [17] of the complement of the binary segmentation result is calculated. The distance transformation assigns for each pixel the distance between that pixel and the

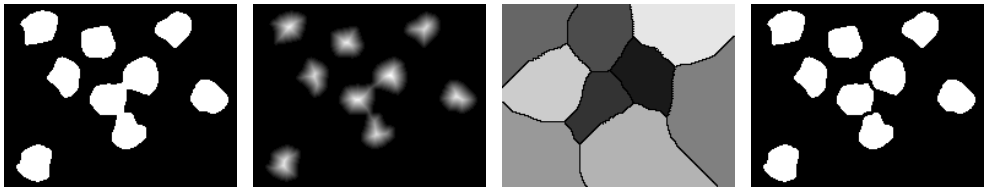

(a) (b) (c) (d)

Figure 2.9: (a) The original binary image. (b) The Euclidean distance transformation of the complement of the original image. (c) The watershed transformation of the complement of the image obtained by applying the h-maxima transformation to the distance transformed image. (d) The region splitting result.

nearest nonzero pixel, and in the resulting image there should ideally be exactly one local maximum for each cell. However, small concavities in the shapes of the cells can result in several local maxima for each cell. Therefore, to prevent over-segmentation, the h-maxima transformation [93] is employed to suppress all local maxima whose height is less than a nonnegative threshold h. Since the watershed transformation begins to flood the surface from each local minimum, it is applied to the complement of the h-maxima transformed image. The resulting watershed lines define the splitting of the clustered foreground objects. Figure 2.9 shows an example of the watershed splitting method for a part of the image in Figure 2.7(c). The region in the middle corresponding to three clustered cells is correctly split into three parts, whereas the other regions corresponding to single cells are not affected by the method.

2.3.6 Morphological filtering

The origins of mathematical morphology lie in the study of the geometry of porous media in the mid-sixties France. Porous media was interpreted as binary data: each point either belongs to a pore or to the matrix surrounding the pores. There are many excellent textbooks on mathematical morphology and its applications in image processing, see, for example, the ones by Serra [88] and Soille [93]. In this section we will cover only the most fundamental morphological operations and refer the reader to these textbooks for further information. Although mathematical morphology can be generalized for multi-valued data and has been applied to gray level images, the following discussion concentrates on binary images. The methods that are described below are therefore suitable for processing binary segmentation results that have been obtained with a segmentation method such as the thresholding, clustering or region growing methods described above.

Mathematical morphology is usually defined in terms of set theory. Within that framework the structuring element is defined as a set that is used to probe the image

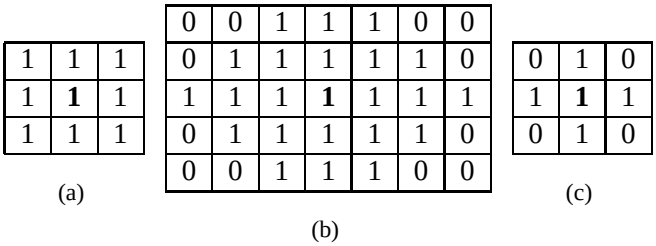

Figure 2.10: Structuring elements.

under study. However, we define the structuring element as a binary-valued mapping of a subset of $\mathbb{Z}^d$.

Definition 2.5 A d-dimensional structuring element with the origin $\mathbf{b}_0 \in \mathcal{D}_B$ is a mapping of a subset $\mathcal{D}_B$ of $\mathbb{Z}^d$ into the couple $\{0, 1\}$ given by

$$B : \mathcal{D}_B \subset \mathbb{Z}^d \longrightarrow \{0, 1\}.$$

The fundamental morphological operations require the definition of an origin for each structuring element. This allows the positioning of the structuring element at a given point. More precisely, a structuring element B at a point $\mathbf{x}$ of an image f indicates that its origin is at $\mathbf{x}$. We restrict ourselves here to flat structuring elements, that is, the dimensionality of the structuring element is always the same as the dimensionality of the image. Usually structuring elements that are symmetric with respect to the origin are used. Examples of structuring elements having these properties are shown in Figure 2.10. The origin of each structuring element is denoted with a boldface font.

The two fundamental morphological operations are erosion and dilation. The eroded value at a given pixel $\mathbf{x}$ of an image f is the minimum value of the image in the window defined by the structuring element B when its origin is at $\mathbf{x}$, that is,

$$[\epsilon_B(f)](\mathbf{x}) = \min_{\mathbf{b} \in \mathcal{D}_B} f(\mathbf{x} + \mathbf{b}). \tag{2.15}$$

Erosion is thus equivalent to the minimum filter having a sliding window that is equivalent to the structuring element B. For example, the erosion of an image by the structuring element shown in Figure 2.10(a) is equivalent to the minimum filter with a 3×3 sliding window.

The dilated value at a given pixel $\mathbf{x}$ of an image f is the maximum value of the image in the window defined by the structuring element B when its origin is at $\mathbf{x}$, that is,

$$[\delta_B(f)](\mathbf{x}) = \max_{\mathbf{b} \in \mathcal{D}_B} f(\mathbf{x} + \mathbf{b}). \tag{2.16}$$

Dilation is thus equivalent to the maximum filter having a sliding window that is equivalent to the structuring element B.

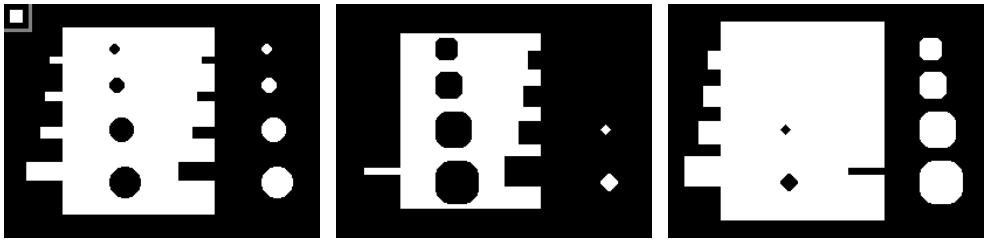

(a) (b) (c)

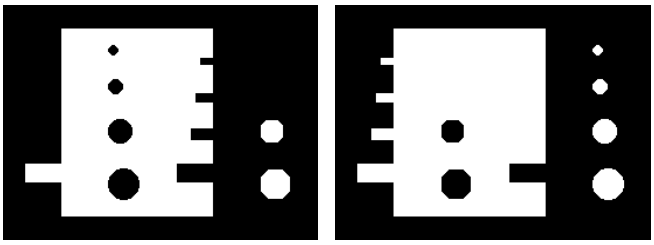

(d) (e)

Figure 2.11: (a) A binary image and a structuring element (top left corner). (b) Morphological erosion of the original image. (c) Morphological dilation of the original image. (d) Morphological opening of the original image. (e) Morphological closing of the original image.

In the case of binary images, the output of erosion is zero unless all the samples in the sliding window are ones, whereas the output of dilation is one unless all the samples are zeros. Erosion shrinks foreground objects and expands their background, whereas dilation expands the foreground objects and shrinks their background. Figure 2.11(a) shows a binary image and a square-shaped structuring element (top left corner). Figures 2.11(b) and 2.11(c) show the erosion and dilation of this image by the square-shaped structuring element.

The morphological opening and closing are morphological operations that are very useful in image processing. Let us first define the reflection of B as its symmetric with respect to the origin. The morphological opening of f by the structuring element B is defined as the erosion of f by B followed by dilation by the reflected structuring element $\check{B}$, that is,

$$\gamma_B(f) = \delta_{\check{B}}(\epsilon_B(f)). \tag{2.17}$$

Erosion first removes all objects in f that cannot contain the structuring element and shrinks all the other objects. When the obtained image is dilated by the reflected structuring element, the objects that have been removed are naturally not recovered. The objects that have not been removed by erosion are restored in such a way that protru-

sions that cannot contain the structuring element remain removed. The morphological opening can thus be used to remove small objects and to smoothen the contours of larger objects. An example is shown in Figure 2.11(d).

The morphological closing of f by the structuring element B is defined as the dilation of f by B followed by erosion by the reflected structuring element $\check{B}$, that is,

$$\phi_B(f) = \epsilon_{\check{B}}(\delta_B(f)). \tag{2.18}$$

Dilation first fills all background structures that cannot contain the structuring element and expands all objects. When the obtained image is eroded by the reflected structuring element, the filled background structures naturally remain filled. The expanded objects are restored in such a way that indentations that cannot contain the structuring element remain filled. The morphological closing can thus be used to fill small holes in the objects and to smoothen the object contours. An example is shown in Figure 2.11(e).

If one has *a priori* knowledge on the morphology of the foreground objects, it is often possible to impose this knowledge on the segmentation results by applying morphological closing and opening operations with a suitable structuring element. For example, cells should not have holes, and therefore holes can be easily filled by a morphological closing by a structuring element that is larger than the holes. Further, the smallest possible area of the cells is often known, and the morphological opening by a structuring element that is smaller than the minimum cell area can be used to remove smaller objects that result from errors in the segmentation. Many cell types have smooth, concave shapes, and opening and closing by a circular structuring element can be applied to smoothen the contours of the recognized objects.

2.4 Feature extraction

In the feature extraction step the relevant quantitative parameters are extracted using the images obtained in the segmentation step. These parameters may include object-specific features such as area, shape, intensity, and color. Image-specific features such as the total number of cells in an image are also often extracted. Extensive lists of possible features can be found in [51] and [80]. To be useful, the features should be invariant to translation and rotation of the objects or images.

It should be noted that feature extraction may aim at directly quantifying certain properties of the objects or at extracting features that are useful in data analysis, see Section 2.6. In the latter case, in addition to features that quantitatively capture the aspects of objects that human experts describe, less intuitive features are often extracted. These features can be related to, for example, the frequency content or texture of objects. They capture information that a human observer may neglect, and may allow improved performance of an automated classifier.

x_4	x_3	x_2
x_5	p	x_1
x_6	x_7	x_8

Figure 2.12: The 3×3 neighborhood of a point p.

2.4.1 Connected component analysis

Usually it is necessary to identify each segmented foreground object individually before features can be extracted. First we need to make a few definitions.

Definition 2.6 Assume the labeling of points (pixels) depicted in Figure 2.12. Then, the points $x_1, x_2, \ldots, x_8$ are the eight-neighbors of p, and the points x_1, x_3, x_5, x_7 are the four-neighbors of p.

Definition 2.7 A sequence of points $y_1, y_2, \ldots, y_n$ is an eight-path (four-path), if y_{i+1} is an eight-neighbor (four-neighbor) of y_i for all $i \in [1, n-1]$.

Definition 2.8 A subset P of pixels from an image f is eight-connected (four-connected) if for every pair p_i, p_j of points in P there is an eight-path (four-path) from p_i to p_j consisting of points in P. If f is a binary image and all points in P have the same value (zero or one), P is said to define an eight-connected (four-connected) component of f.

The individual identification of segmented foreground objects can be done by connected component labeling. The same label is set for pixels belonging to the same connected component, whereas pixels belonging to different connected components get different labels. Integer labels are usually used, and the background usually retains the zero label. A method for labeling connected components can be found in, for example, [81] as well as in numerous textbooks on digital image processing.

Many features are very easy to extract from a labeled image. For example, assuming correct segmentation, the number of labels corresponds to the number of foreground objects. Measurements can be performed separately for each foreground object by considering only points that have the same label. For example, the areas of the objects can be directly obtained by looking at the histogram of the labeled image. It should be noted that the considered connectivity has an effect on the extracted features. Usually eight-connected components are considered.

Because the field of view is finite in a digital image, it may contain only a part of some foreground objects. These objects can be detected by finding objects that touch the edges of the image. In feature extraction it is important to handle these objects appropriately. If the number of objects is the only feature to be extracted, the standard approach is to include in the count objects that touch two edges (and of course objects that do not touch any edge), for instance the top and the left, and to ignore those that

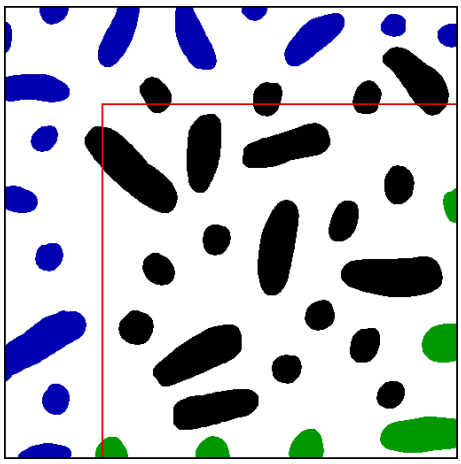

Figure 2.13: The use of a guard frame for unbiased feature extraction. Features are extracted only from the objects marked black, whereas objects touching the bottom or right edges (green) as well as objects in the guard frame (blue) are ignored.

touch the other two edges [82]. This approach can be used to find an unbiased estimate for the number of objects per unit area.

If features such as the area, shape, or intensity of the objects are extracted, a more complicated procedure may be needed. It is clear that such features cannot be extracted from an object that touches any of the edges of the image, because the object is not completely visible. If only objects that do not touch any edge are measured, the proportions of small and large objects are wrong, because it is more likely that a large object will touch an edge. Unbiased features can be extracted by dividing the image into an active region and a guard region. The idea is illustrated in Figure 2.13, in which the border between the active region (bottom right) and the guard region is marked with a red line. As before, objects that touch the bottom and right edges (marked green) are not counted or measured. The same applies to objects that lie entirely within the guard frame (marked blue), irrespective of whether they touch the top or left edges or not. Only objects that lie entirely in the active region or cross the edge between the guard frame and the active region (marked black) are counted and measured. Since the guard frame has to be large enough so that it is not possible for an object to extend from the active region across the guard region to the edge of the image, in applications with large objects the active region may have to be much smaller than the guard region.

2.4.2 Thinning

The extraction of certain features may require further image processing. For example, if the lengths of elongated objects need to be extracted, the objects must be reduced to arcs that are one pixel in width. The reduction process is generally referred to as thinning, and the result of thinning an object is the skeleton of the object. A wide range

of different thinning methods can be found in the literature. They produce slightly different skeletons, and are often designed with a particular application in mind. A comprehensive review of thinning methods can be found in [58]. Some of the more recent studies, such as the ones reported in [20] and [90], have concentrated on thinning in the presence of different types of noise. Thinning methods are usually divided into two classes: iterative and non-iterative. Iterative methods delete successively layers of pixels on the boundary of the object until only a skeleton remains. Non-iterative methods produce a center line of the object directly in one pass. This can be accomplished by, for example, medial axis or distance transformations.

The skeletons obtained with a thinning method may contain spurious arcs, that is, short arcs that are not topologically equivalent to the underlying object. The spurious arcs result from small protrusions and indentations in the binary image obtained after segmentation. The removal of the short arcs is referred to as pruning. It can be achieved by, for example, iteratively removing endpoints of the skeletons until a given number of iterations is reached.

2.5 Validation and quality control

In the validation step the goal is to confirm that the features extracted in the previous step are correct. Validation is strongly related to the more general concept of performance evaluation, see, for example, [104]. Validation usually starts with a visual evaluation of the results, that is, segmentation results are compared with the original images to see whether the segmentation seems to have been done correctly. However, visual evaluation is not a well-defined way of validating image analysis results. It is also always subjective. A ground truth evaluation should therefore be made when possible, that is, images for which the correct features are known should be used in order to make an assessment of how well the image analysis method can match these results.

Traditionally the ground truth is obtained by manual inspection of the samples under the microscope. However, such a manual quantification may not be completely accurate [100]. One way of mitigating this problem is to let several experts repeat the manual quantification several times. An average of these manual quantifications can be assumed to be more accurate than a single manual quantification, and the variance gives a measure of the reliability of the ground truth obtained in this way. Because a large number of samples or images need to be quantified manually in order to have a significant amount of ground truth data, the disadvantage of the above approach is that it is very labor-intensive and can therefore be slow and expensive. Although factors such as irregularities in the obtained images and physical fatigue can cause problems in counting the number of cells in a sample, it is a task that in principle can be accomplished by visual inspection with the microscope. Many other parameters, such as areas or lengths, are much more difficult to quantify manually, and an accuracy that is needed for ground truth data cannot be obtained.

Fully accurate ground truth data can be obtained by using simulated images. In principle the cells in the images can be of any type and any kind of features can be associated with them. A preliminary step towards validation based on simulation was taken in [60], in which simulation of fluorescent microscope images of cell populations was considered. The user can specify a number of parameters, and an image is created based on these parameters. For example, it is possible to use the simulator to create images for which the number of cells in the image is known. These images can be used as ground truth for methods that extract the number of cells in the image. In order for the ground truth to be useful, the simulated images must be similar enough to real experimental images. In order to accomplish this, the simulator has parameters that control factors such as cell size, cell shape, cell texture, the color of the stain, clustering of the cells, uniformity of illumination, camera noise, and so on.

Whether simulated or real images are used as ground truth images, the set of ground truth images should be representative of the new images that will be encountered later when the image analysis method that is being validated will be used. It is also a good idea to perform some worst-case testing, that is, to test what happens when the image contains some rare or unusual features.

An alternative to ground truth validation is to let one or more experts do repeat manual quantifications of the image data. If the variation between these manual quantifications is as large as it is between each of the manual quantifications and the automated quantification, we know that the the accuracy of the automated method is comparable to manual quantification.

Quality control is an issue related to validation. The idea is to make sure that features are extracted only from those objects at which the image quality is sufficient. For example, cells in a cell population may be in different focal planes, and features should be extracted only from those cells that are in good enough focus. It is also possible that the image includes artefacts that should be ignored even though they are similar to cells or other foreground objects.

Quality control can be done by comparing each segmented object with objects that are known to be segmented correctly. The objects that may or may not be segmented correctly form a test data set, and the objects that are known to be segmented correctly form a ground truth data set. The comparison between objects from these sets is done in a multi-dimensional feature space. Let us denote the feature vector of an object from the test data set by $\mathbf{a}$, and the mean of the feature vectors of the objects from the ground truth data set by $\bar{\mathbf{a}}$. Then, the new object is classified as "valid" if the distance between $\mathbf{a}$ and $\bar{\mathbf{a}}$ is less than a predefined threshold. Otherwise it is classified as "not valid", and the object is not included in the subsequent analysis. In [107] the Mahalanobis distance $d_M(\bar{\mathbf{a}}, \mathbf{a}_i)$ given by Equation (2.13) was used as the distance measure, but other distance measures may be used as well. A large threshold value increases the risk of artefacts or objects in poor focus being included in the subsequent analysis, whereas a small threshold increases the risk that well focused objects are excluded from the analysis. We can say that in the former case there can be false positives and in the latter

case there can be false negatives. There are applications in which false negatives are not a significant problem. For example, if the goal is to find properties of individual cells and there is a large supply of cells, it is best to quantify only well-focused cells, because otherwise the quantified cell-specific features may be inaccurate. However, in applications in which the number of cells per unit area or other image-specific features are quantified, false negatives are just as problematic as false positives.

2.6 Data analysis

The numerical data produced in the feature extraction step may not be the desired end result. Instead, the goal may be to extract some specific higher level information on the objects recognized in the segmentation step. For example, the goal may be to find the percentages of different types of objects. In other studies test samples are compared with control samples. For example in studies related to drug discovery test samples are treated with different agents and compared with control samples so that the effect of the agent can be quantified. In these studies multivariate statistical analysis techniques are typically used. In comparative studies the important question is whether the effects observed in the test samples are statistically significant. This can be achieved by drawing confidence intervals and by performing statistical significance tests.

An enormous amount of methods for performing data analysis can be found in the literature, see, for example, [51] and [65] as well as the references in these papers. Typically the first step is to reduce the dimensionality of the problem by selecting those features that are most suitable for the problem. Both supervised and unsupervised methods can thereafter be used for classification. A validation step is also required to determine the accuracy of the classifier. However, the implementation of the data analysis step is outside of the scope of this thesis.

Chapter 3

Case studies

This chapter describes four case studies that have been published in the enclosed publications. The case studies apply the principles described in Chapter 2. The solutions to the image analysis problems require the application of existing image analysis methods as well as the development of new methods or new combinations of image processing steps. The aim of the publications has been to develop image analysis methods that are general enough so that they can be applied in a wide range of similar image analysis problems. The applications of the publications cover a substantial range of different situations, and the developed methods provide a good basis for taking on new applications within the field of biomedical microscopy imaging.

3.1 Quantification of *in vitro* angiogenesis

Angiogenesis is the formation of new blood vessels from pre-existing vasculature. It plays an important role in embryonic development, tissue repair and wound healing, tumor growth and metastasis, and various vascular diseases [6, 35, 79]. Publication I proposes an image analysis method for quantifying angiogenesis. It is designed for *in vitro* angiogenesis assays that are based on co-culturing endothelial cells with fibroblasts. Publication II uses the method proposed in Publication I to compare quantitatively the global properties of vascular networks grown with an *in vitro* angiogenesis assay with the global properties of networks obtained with discrete, stochastic growth models.

The motivation of Publication I is in drug discovery. The growth, invasion, and metastasis of most solid tumors are dependent on angiogenesis. Therefore, one of the strategies for the treatment of cancer is to inhibit angiogenesis by using specific anti-angiogenic agents [33, 55]. The first anti-angiogenic agents have been recently approved for clinical use in several countries and currently there are many angiogenic inhibitors in clinical trials [34]. To be able to find anti-angiogenic agents, the stimulatory and inhibitory effects of the different agents need to be quantified. Before a potential drug is tested on animals or humans, it can often be tested in an *in vitro* ex-

periment. Each potential agent is added to the *in vitro* experiment and the effects are observed, preferably by automated image analysis. Agents that do not have the desired inhibitory effect are removed from further testing. The same applies to agents that are, for example, toxic or otherwise have undesired side-effects.

Some papers present computer-assisted methods for quantification of angiogenesis, see, for example, [57, 102]. In these papers general purpose image processing software is used for the segmentation task. Automated methods that use such general purpose software have also been proposed, see, for example, [15]. In [28] a fully automated quantification method for *in vitro* assays based on the chorioallantoic membrane is presented. In addition, a lot of work on quantification of blood vessels in different contexts can be found in the literature. Many papers consider the segmentation of retinal blood vessels, see, for example, [42, 50, 97]. There are also a large number of papers on blood vessels segmentation in angiograms, see, for example, [21, 25]. The segmentation problems in these papers are very similar to the one considered in Publication I.

3.1.1 Image acquisition

The angiogenesis experiment was done with the TCS Cellworks Angiokit (Buckingham, UK), a commercially available *in vitro* angiogenesis assay [14]. The assay utilizes a fibroblast matrix seeded with endothelial cells. Each well of the assay plate can be used to test a condition. Immunostaining is used to stain the endothelial cells that form the tubules that are grown with the assay. Each well was imaged with a bright field microscope using a resolution of 1300×1030 pixels and 8 bits per pixel.

Four assay plates, each consisting of 24 wells, were used to examine the effects of commercially available purified insulin-like growth factor-binding proteins (IGFBP) 1 through 5. In addition, each plate contained negative and positive control wells. The negative controls were obtained by treating the well with 20 μM suramin, an anti-angiogenic drug [38]. The positive controls were obtained by treating the well with 2 ng/ml vascular endothelial growth factor (VEGF). Each plate also contained control samples with no treatment.

3.1.2 Pre-processing

The first step of the image analysis method proposed in Publication I is the correction of nonuniform illumination. The additive illumination model is assumed, and the nonuniformity component ξ_a is found with a separated second order polynomial fit.

Let us first consider a kth order polynomial of the form

$$p(m) = a_0 + a_1 m + \ldots + a_k m^k. \tag{3.1}$$

Given N data points (m_i, b_i), the polynomial least squares fit can be found by finding

the coefficients a_i from the equation

$$\begin{bmatrix} b_1 \\ b_2 \\ \vdots \\ b_N \end{bmatrix} = \begin{bmatrix} 1 & m_1 & m_1^2 & \dots & m_1^k \\ 1 & m_2 & m_2^2 & \dots & m_2^k \\ \vdots & \vdots & \vdots & \ddots & \vdots \\ 1 & m_N & m_N^2 & \dots & m_N^k \end{bmatrix} \begin{bmatrix} a_0 \\ a_1 \\ \vdots \\ a_k \end{bmatrix}. \tag{3.2}$$

In matrix notation this is given by

$$\mathbf{b} = \mathbf{M}\mathbf{a}, \tag{3.3}$$

where the matrix $\mathbf{M}$ is also known as the Vandermonde matrix and uses the vector $\mathbf{m} = [m_1, m_2, \dots, m_N]$ as the basic building block. The least squares solution for $\mathbf{a}$ is given by

$$\mathbf{a} = (\mathbf{M}^{\mathrm{T}}\mathbf{M})^{-1}\mathbf{M}^{\mathrm{T}}\mathbf{b}, \tag{3.4}$$

where $(\mathbf{M}^{\mathrm{T}}\mathbf{M})^{-1}\mathbf{M}^{\mathrm{T}}$ is the pseudoinverse of $\mathbf{M}$. The fitted polynomial can then be evaluated by using Equation (3.3).

Let us use a matrix representation for images. Then we denote the image f by a matrix $\mathbf{F}$. Let us assume that the size of the image matrix is $M \times N$. The separated kth order polynomial least squares surface fit on the image is then done as follows. We first fit a kth order polynomial on each horizontal line $\mathbf{f}_j$ of the image by

$$\mathbf{w}_j = \mathbf{M}(\mathbf{M}^{\mathrm{T}}\mathbf{M})^{-1}\mathbf{M}^{\mathrm{T}}\mathbf{f}_j, \tag{3.5}$$

where $\mathbf{m} = [0, 1, \dots, N-1]$. Then we form an image $\mathbf{W}$ from the polynomials $\mathbf{w}_j$ and fit a kth order polynomial on each vertical line $\mathbf{w}_i$ of that image by

$$\mathbf{b}_i = \mathbf{M}(\mathbf{M}^{\mathrm{T}}\mathbf{M})^{-1}\mathbf{M}^{\mathrm{T}}\mathbf{w}_i, \tag{3.6}$$

where $\mathbf{m} = [0, 1, \dots, M-1]$. The background estimate image $\mathbf{B}$ is then formed from the polynomials $\mathbf{b}_i$, and can also be denoted by $b(m, n)$, where $m \in \{0, 1, \dots, M-1\}$ and $n \in \{0, 1, \dots, N-1\}$.

Figure 3.1 shows an example of correction of nonuniform illumination using the separated least squares fit. After the background estimate is obtained as presented above, the correction is done using Equation (2.9) with $\xi_a = b$ and $C_a = \max[b(m, n)]$. The image shows a well from an *in vitro* angiogenesis assay, and is part of the study of Publication I. Since the original image shown in Figure 3.1(a) has a vignetting effect, a second order polynomial fit is used to remove it. The vignetting effect can be most clearly seen in the thresholding result in Figure 3.1(b): because the background is darker in the corners of the image than elsewhere, the thresholding result is unacceptable in the corner areas. The result after correction of nonuniform illumination is shown in Figure 3.1(c) and the global thresholding result in Figure 3.1(d) shows that a sufficiently uniform background is achieved.

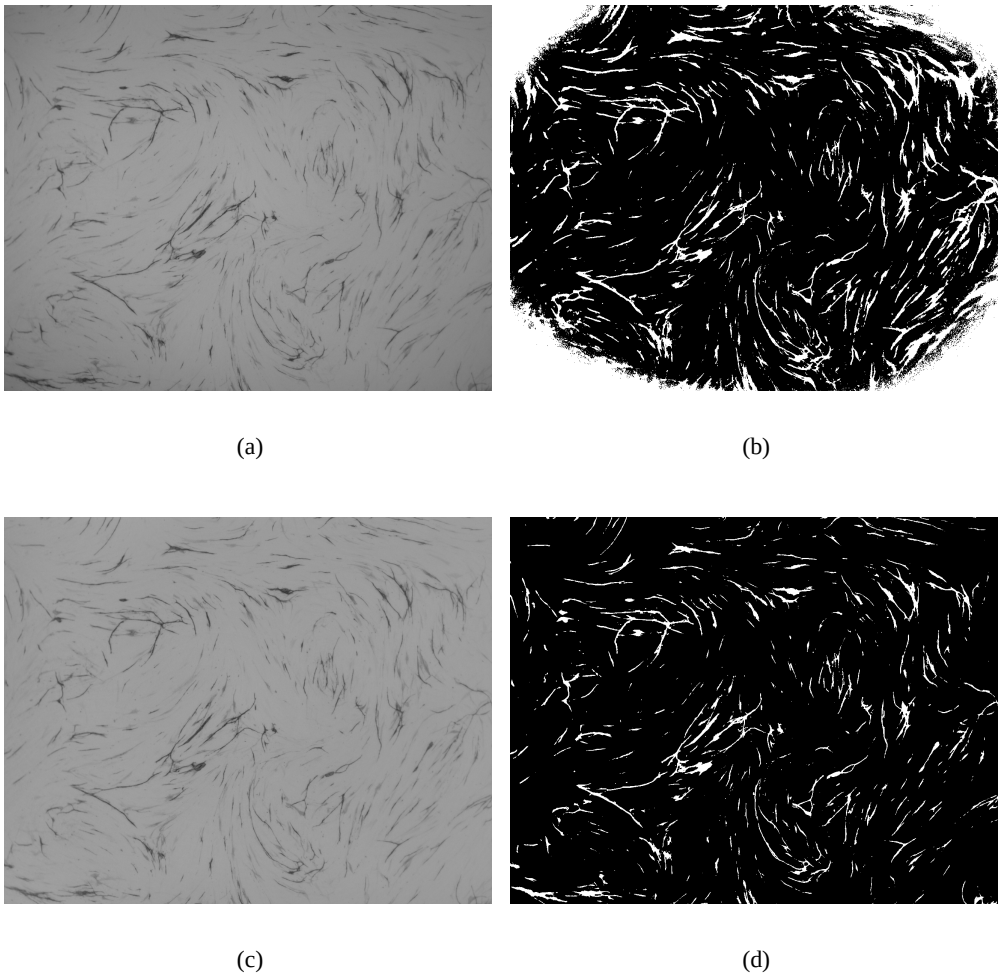

(a) (b)

(c) (d)

Figure 3.1: (a) An image of an *in vitro* angiogenesis assay with nonuniform illumination. (b) The original image after global thresholding with the threshold value 135. (c) The original image after correction of nonuniform illumination by a separated polynomial least squares background fi t. The additive illumination model is assumed. (d) The original image after correction of nonuniform illumination and global thresholding with the threshold value 135.

As explained in Section 2.2.2, the correct model for correction of nonuniform illumination depends on the sensor response function of the camera. The additive model used above is correct for a logarithmic device. Since the camera that was used to obtain the angiogenesis images probably is not logarithmic, we tested correction of nonuniform illumination with the multiplicative model, and found that the model choice does not have a significant effect on the results. For example, Figure 3.2(a) shows the image in Figure 3.1(a) after correction of nonuniform illumination by Equation 2.10 with

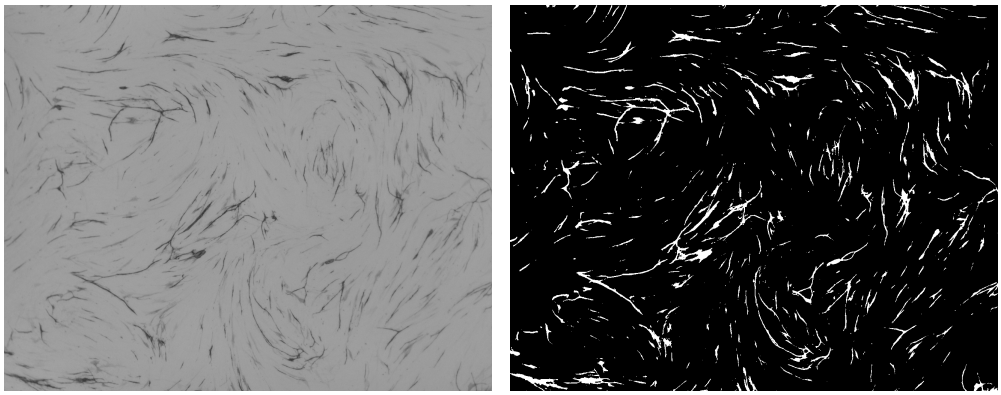

(a) (b)

Figure 3.2: (a) The image in Figure 3.1(a) after correction of nonuniform illumination by a separated polynomial least squares background fi t. The multiplicative illumination model is assumed. (b) The original image after correction of nonuniform illumination and global thresholding with the threshold value 135.

$\xi_a = b$ and $C_m = \max[b(m,n)]$. Figure 3.2(b) shows the respective global thresholding result. These results are very similar to the ones obtained using the additive illumination model, see Figures 3.1(c) and 3.1(d).

The above correction method does not take into account the fact that some of the pixel values do not represent the background. In the above example, blood vessels are much darker than the background and can be thought of as outliers. Since the least squares fit is sensitive to outliers, they may have an undesired effect on the fit. If the outlier values are distributed approximately evenly in the data to be fitted, they effectively cause the fit to be slightly below the actual background pixel values, see Figure 3.3. Such a consistent bias does not have any effect on the background correction result, because the maximum value of the background estimate b was used as the normalization coefficients C_a and C_m in Equations (2.9) and (2.10). In both cases, this selection has the property that the intensity value of the point or points with highest illumination remains intact, and the intensity values of the other points are increased.

If the outlying values are not distributed evenly, the outliers may render the least squares fit unusable. As a solution, one could select the grid points that are used in the fitting procedure in such a way that object pixels are excluded. In the case of bright objects on a dark background one can calculate the standard deviation of all pixel values and mask away pixels that deviate more than a constant number of standard deviations from an initial background estimate [64]. In the case of dark objects on a bright background one can use the same criterion on the complement image. Another approach is to make the selection of grid points locally by dividing the image into small

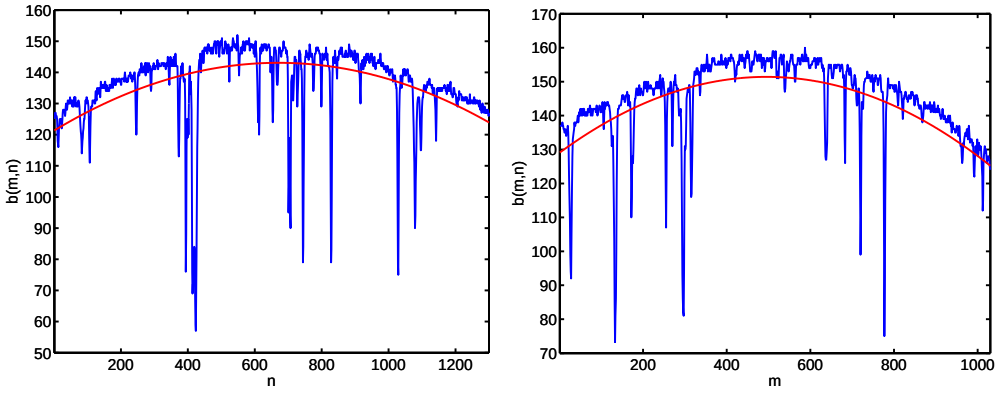

(a) (b)

Figure 3.3: (a) The intensity profiles of the horizontal line $m = 900$ from the image in Figure 3.1(a) (blue) and from the polynomial least squares fit (red). (b) The intensity profiles of the vertical line $n = 300$ from the image in Figure 3.1(a) (blue) and from the polynomial least squares fit (red).

non-overlapping neighborhoods and selecting the brightest pixel in each neighborhood as a grid pixel [82]. However, in the former approach the constant number of standard deviations and in the latter approach the neighborhood size depend on the image, and thus these correction methods are not fully automated.

Since with image data the outliers result from high or low pixel values, they affect the one-dimensional intensity profiles only in the vertical direction. Thus, we can use robust M-estimators [45] to make a robust fit in a fully automated fashion. M-estimators can be thought of as a generalization of least-squares estimation. Let r_i be the residual of the ith data point, that is, the difference between the ith data point and its fitted value. Least squares estimation tries to minimize $\sum_i^N r_i^2$, which is unstable to outliers in the data. Replacing the cost function r_i^2 by a general function $\rho(r_i)$ of the residual yields

$$\min \sum_i^N \rho(r_i). \tag{3.7}$$

This defines the general class of M-estimators. Some choices for $\rho(r_i)$ result in a robust estimator. Here we use the the Tukey cost function, which is defined by

$$\rho(r_i) = \begin{cases} \frac{c^2}{6}\left(1 - \left[1 - (r_i/c)^2\right]^3\right), & \text{if } |r| \le c, \\ \frac{c^2}{6}, & \text{if } |r| > c, \end{cases} \tag{3.8}$$

where c is a tuning constant that affects the asymptotic efficiency of the M-estimator. The Tukey M-estimator has the nice property that it totally removes the influence of

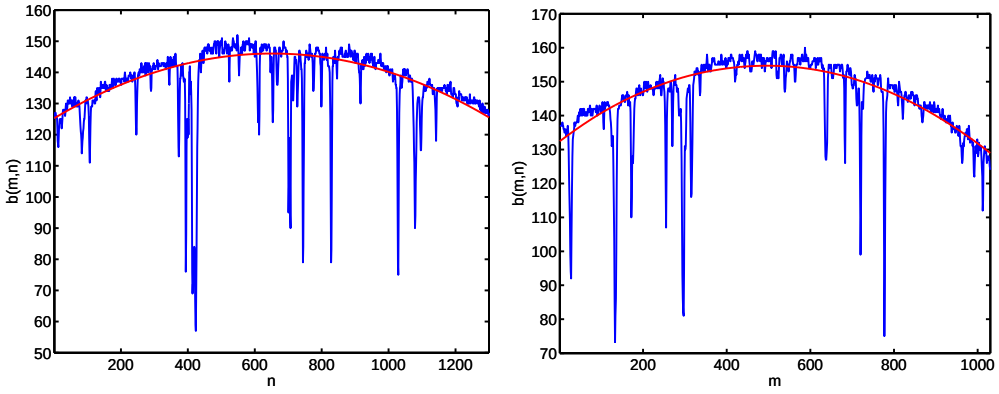

(a) (b)

Figure 3.4: (a) The intensity profiles of the horizontal line $m = 900$ from the image in Figure 3.1(a) (blue) and from the polynomial Tukey M-estimator fit (red). (b) The intensity profiles of the vertical line $n = 300$ from the image in Figure 3.1(a) (blue) and from the polynomial Tukey M-estimator fit (red).

all points whose residuals grow beyond c in the absolute value. Typically $c = 4.6851$ is used, resulting in 95% asymptotic efficiency. This value of the tuning constant is suitable for the typical dynamic ranges of digital images. Therefore a nonparametric method can be obtained by fixing c to this value.

Figure 3.4 shows the same intensity profiles as are shown in Figure 3.3, only now the Tukey M-estimator fit is shown. Clearly now the fit better follows the intensity values of the background pixels from the original image, that is, the outliers do not have a serious effect on the fit. The only disadvantage of the robust M-estimator method is that it is computationally more complex than the least squares method.

3.1.3 Segmentation

In addition to actual tubules, the obtained images contain tubule-like fibroblast structures. These structures have a similar appearance to tubules, but are in general lighter. However, some parts of tubules can be as light as fibroblasts, and therefore segmentation cannot be achieved by global thresholding. Instead, the segmentation is performed with hysteresis thresholding [18]. The method is sometimes called double thresholding.

The first step of hysteresis thresholding is to threshold the image separately with two different thresholds. The two thresholds define two different ranges of gray level values for the foreground, one being included in the other. The foreground objects of the binary image corresponding to the wider range are candidates for foreground objects in the hysteresis thresholding result. The foreground pixels defined by the nar-

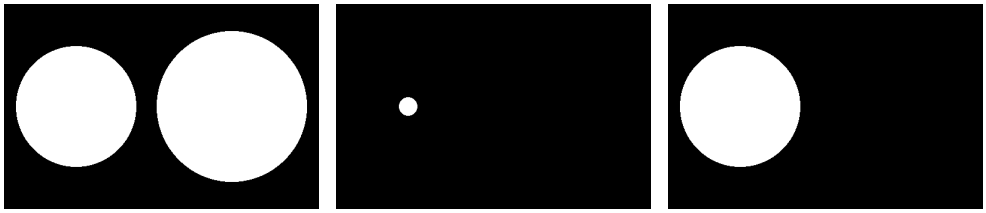

(a) (b) (c)

Figure 3.5: The principle of hysteresis thresholding. (a) Wide thresholding result. (b) Narrow thresholding result. (c) Hysteresis thresholding result.

rower range are then used as seeds. Those candidate objects that overlap with a seed pixel are marked as foreground objects. Figure 3.5 illustrates the idea.

In Publication I the threshold corresponding to the wider range was obtained with Otsu's method [75]. After thresholding some of the recognized tubules and fibroblast structures are filled with a morphological closing by a 3×3 square structuring element. The midpoint of the range of gray level values of the input image was used as the threshold corresponding to the narrower range. Figure 3.6(a) shows a 280×240 pixel fraction of one of the test images. With this image Otsu's method gives the threshold value 146, and the resulting wide thresholding result is shown superimposed in red color on the original image in Figure 3.6(b). It can be seen that many of the fibroblast structures get incorrectly recognized as foreground pixels. The threshold corresponding to the narrower range is 118, and the respective image is shown in Figure 3.6(c). The hysteresis thresholding result is shown in Figure 3.6(d). Now only the darkest structures are recognized as tubules.

3.1.4 Feature extraction

The segmentation step results in a binary representation of the tubules. There are typically networks of connected tubules, which are referred to as tubule complexes in Publication I. The parameters to be extracted are the areas of the tubule complexes, the lengths of the tubule complexes, and the numbers of junctions in the tubule complexes. The area of a tubule complex is measured in pixels by counting the number of pixels in its binary representation.

In order to be able to measure the lengths of tubules and to detect junction points, the tubules must be thinned so that they are exactly one pixel in width. This is done by Algorithm 1 from the paper by Guo and Hall [44]. It is an iterative thinning method that can be implemented efficiently using look-up tables. Because the obtained skeletons contain spurious arcs, the skeletons need to be pruned. Pruning is done with a method that removes arcs that are shorter than a given threshold without shortening the other

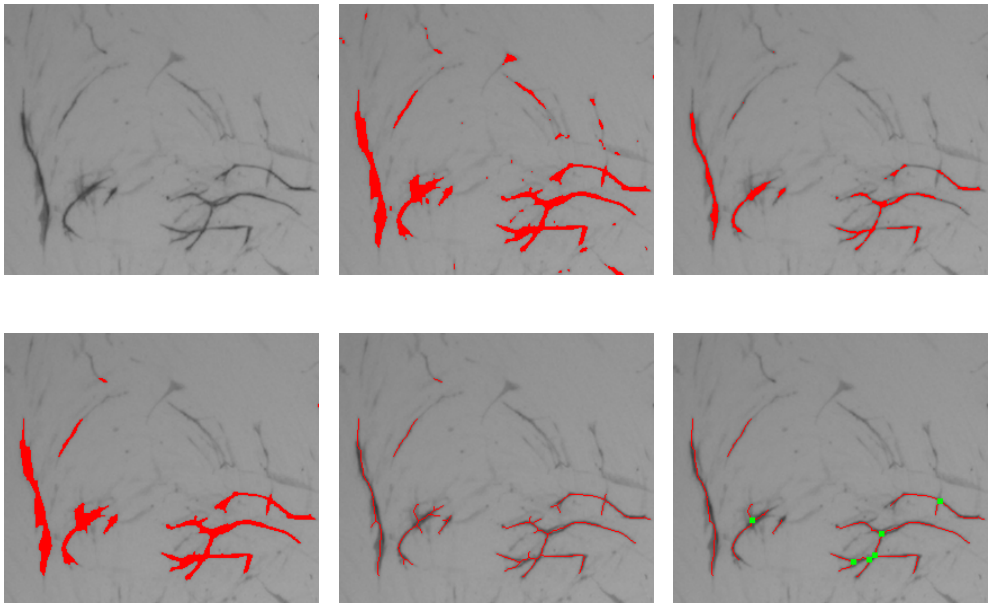

Figure 3.6: (a) A fraction of an image of an *in vitro* angiogenesis assay after correction of nonuniform illumination. (b) Wide thresholding result. (c) Narrow thresholding result. (d) Hysteresis thresholding result. (e) Skeleton of the hysteresis thresholding result. (f) Pruned skeleton and junctions.

arcs. The details of the method can be found in Publication I. After thinning, the length of a tubule complex can be obtained by $L = N + (\sqrt{2} - 1)N_d - 1$, where N is the total number of pixels in the skeleton of the tubule complex and N_d is the number of diagonally connected pairs of pixels. Junction points can be detected by finding those points whose eight-neighbors form more than two four-connected components. Figure 3.6(e) shows the skeleton corresponding to the segmentation result shown in Figure 3.6(d). Figure 3.6(f) shows the pruned skeleton and the junction points (green squares).

3.1.5 Validation

The proposed quantification method was tested with a set of 24 control images. There were 7 negative controls (suramin), 9 positive controls (VEGF), and 8 no treatment controls. The controls come from 4 different plates. Since the number of tubule complexes varies significantly between the images, we compare the mean lengths and areas of tubule complexes and the mean numbers of junctions per tubule complex. The quantification results can be seen in Table 3.1. The lengths and areas of tubule complexes are measured in pixels, since this is sufficient for the purpose of comparing the results obtained with different treatments.

Table 3.1: Quantification of 24 control wells from an *in vitro* angiogenesis assay.

			length		area		junctions	
treatment	plate	complexes	total	mean	total	mean	total	mean
none	A	190	15431.4	81.2	61851	325.5	118	0.62
none	A	208	16347.1	78.6	63633	305.9	130	0.63
none	B	173	14440.4	83.5	56818	328.4	117	0.68
none	B	173	13418.8	77.6	54334	314.1	99	0.57
none	C	319	16824.7	52.7	77837	244.0	116	0.36
none	C	298	16519.8	55.4	80703	270.8	150	0.50
none	D	207	14611.0	70.6	87793	424.1	115	0.56
none	D	283	24999.0	88.3	132607	468.6	303	1.07
suramin	A	121	3769.1	31.2	17073	141.1	5	0.041
suramin	A	92	3109.9	33.8	14489	157.5	9	0.098
suramin	B	100	3105.0	31.1	13630	136.3	2	0.020
suramin	C	259	9669.9	37.3	47625	183.9	51	0.20
suramin	C	241	7181.3	29.8	34457	143.0	33	0.14
suramin	D	183	7677.4	42.0	36387	198.8	48	0.26
suramin	D	51	5341.8	35.4	27210	180.2	15	0.10
VEGF	A	164	18550.2	113.1	80249	489.3	171	1.04
VEGF	A	199	26959.5	135.5	117909	592.5	329	1.65
VEGF	B	193	22844.2	118.4	102048	528.8	298	1.54
VEGF	B	164	26212.6	159.8	117450	716.2	379	2.31
VEGF	C	283	27321.0	96.5	117562	415.4	299	1.06
VEGF	C	344	30609.1	89.0	128122	372.5	320	0.93
VEGF	D	334	50577.1	151.4	251090	751.8	992	2.97
VEGF	D	278	37788.6	135.9	204936	737.2	601	2.16
VEGF	D	305	42684.2	140.0	217492	713.1	725	2.38

The obtained quantification results are similar for duplicate (same treatment) wells. Moreover, we observe the expected results when the wells with suramin and VEGF treatments are compared against the wells with no treatment. There are fewer tubule complexes in the wells treated with suramin than in the wells with no treatment. Further, the tubule complexes are much shorter and smaller than in the wells with no treatment. There are also fewer junctions. For the wells treated with VEGF, the quantification shows increased mean tubule complex lengths and areas as compared with wells with no treatment. The mean numbers of junctions are also higher.

Figure 3.7 shows each of the 24 wells in a two-dimensional feature space. The horizontal axis is the mean length of the tubule complexes, and the vertical axis is the mean number of junctions per tubule complex. Wells with suramin treatment are represented by squares, wells with VEGF treatment are represented by upward triangles,

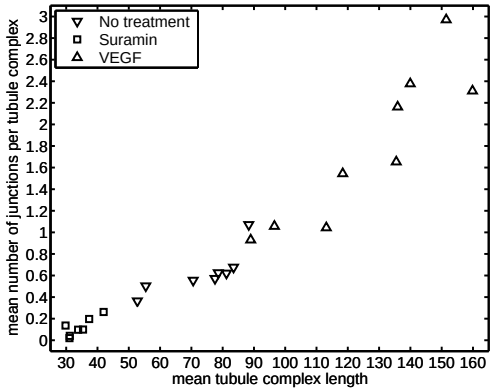

Figure 3.7: A representation of 24 control wells from an *in vitro* angiogenesis assay in a two-dimensional feature space.

and wells with no treatment are represented by downward triangles. The three classes separate well in the feature space.

3.1.6 Data analysis

Effects of insulin-like growth factor-binding proteins

The members of insulin-like growth factor binding protein (IGFBP) family have been implicated in diverse cellular functions. They are secreted proteins that are present in circulation, with some of the members abnormally expressed in tumors. The work presented in [31] uses the image analysis method presented in Publication I to show that different members of the IGFBP family have distinct effects on angiogenesis. The experiment included IGFBPs 1 through 5. The endothelial cells were treated in triplicate wells for 11 days with 2 μg/ml, 0.2 μg/ml, and 0.02 μg/ml of each purified protein mixed in the medium. We also included two wells each of 2 ng/ml VEGF as a positive control, 20 μM suramin as a negative control, and medium only as a no treatment control.

The number of junctions, number of tubule complexes, total tubule length, and mean tubule length were quantified for each well. The results showed that the IGFBP1-treated wells showed effects similar to the angiogenesis inhibitor suramin in terms of all four measured quantities. IGFBP2 and IGFBP4 showed an effect similar to VEGF in terms of these quantities, whereas IGFBP3 and IGFBP5 showed no significant effects.

Mathematical modeling of angiogenesis

Angiogenesis involves interactions among angiogenic factors, inhibitors, and regulators at molecular, cellular, and tissue levels. To understand such a complicated process, the experimental approach must be combined with mathematical modeling. The experimental approach enables us to investigate isolated factors and simple interactions, while

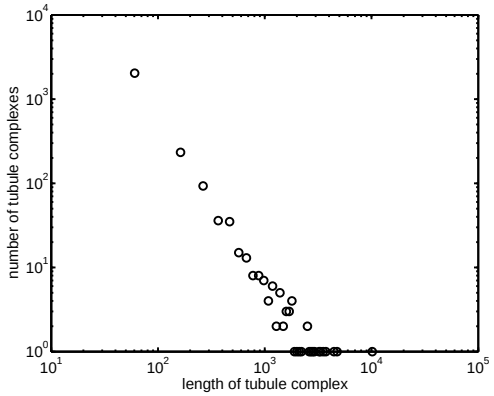

Figure 3.8: The power law behavior of tubule complex lengths in *in vitro* angiogenesis treated with VEGF.

through mathematical modeling we can understand the large-scale emergent properties of angiogenesis from a systems perspective. Indeed, several mathematical models of angiogenesis have been developed, see, for example, [19, 71, 74, 76].

Publication II compares the global properties of vascular networks grown with the TCS Cellworks Angiokit with the global properties of networks obtained with discrete, stochastic growth models. The model classes that are investigated are invasion percolation [103] and diffusion limited aggregation [105]. Both models have several parameters that control their behavior, and the simulations are made with different sets of parameters to obtain networks with different properties. The networks grown with the TCS Cellworks Angiokit are quantified with the image analysis method presented in Publication I. It is found that invasion percolation is better than diffusion limited aggregation at matching experimental data.

Tubule complex length distribution

The tubule complex length distribution in the experimental angiogenesis data used in Publication II follows a power law. This data set contains the tubule complex lengths of 2529 tubule complexes obtained from 9 different wells treated with VEGF. The power law behavior suggests that a power law distribution provides optimal efficiency of blood transfer. One possible explanation for the power law behavior is that large tubule complexes have more potential branching points than small tubule complexes. Since tubule complexes can grow either by branching or at the endpoints of existing branches, large tubule complexes have more potential to grow than small tubule complexes. Thus, the larger a tubule complex is, the faster it grows. This is akin to preferential attachment, which is one of the mechanisms known to give rise to power law degree distributions in networks [10]. The histogram of the tubule complex length data is plotted on a log-log scale in Figure 3.8.

3.2 Quantification of *in vitro* invasion

Tumor cells have the ability to invade surrounding tissues. Highly malignant cells also have the ability to give rise to distant metastases by transversing vascular tissues and migrating through the blood stream. The ability of cancer cells to invade into the surrounding tissue correlates with cellular malignancy and the ability of the cancer to metastasize.

The invasive capability of cells can be studied with *in vitro* invasion assays. Most of them are based on an invasion chamber that consists of two compartments that are separated by a porous membrane, see, for example, [2, 78]. The cells are placed in the upper compartment, and they invade through the pores of the membrane to the lower compartment. The remaining cells are removed from the upper compartment, and the invaded cells in the lower compartment are stained and observed with a microscope.

The applications of *in vitro* invasion assays include the assessment of the invasive potential of tumor cells [96] as well as of some developmental normal cells [26] and the assessment of inhibition of tumor cell invasion by inhibitory drugs [85]. The work presented in [86] is one of the few attempts to apply image analysis methods for quantifying *in vitro* invasion assays. However, the image processing method presented in that paper consists merely of global thresholding with a predefined threshold. Although this simple method seems to provide good results for the custom assay that is described in the paper, it does not provide good results with most other assays. Publication III proposes an image analysis method for quantifying *in vitro* invasion.

3.2.1 Image acquisition

The invasion experiments were conducted with the BD BioCoat Matrigel Invasion Chamber (Bedford, Mass., USA), a commercially available *in vitro* assay that uses matrigel as a coating on top of the porous membrane [2]. The invaded cells were stained with the Diff-Quik stain [92]. The assays were then imaged with a bright field microscope using a resolution of 1300×1030 pixels and 8 bits per pixel. Imaging was done in such a way that the rectangular image contains the whole circular well. To facilitate correction of nonuniform illumination, an image of an empty slide was taken in each imaging session.

3.2.2 Pre-processing

The first step of the image analysis method proposed in Publication III is the correction of nonuniform illumination. The additive illumination model is assumed, and the image taken of an empty slide is used as the nonuniformity component ξ_a. It is important that the empty image is taken with the same illumination, microscope, and camera settings as the assay images to be quantified.

Figure 3.9 shows an example of correction of nonuniform illumination in one of the images used in the study of Publication III. The original image in Figure 3.9(a) as

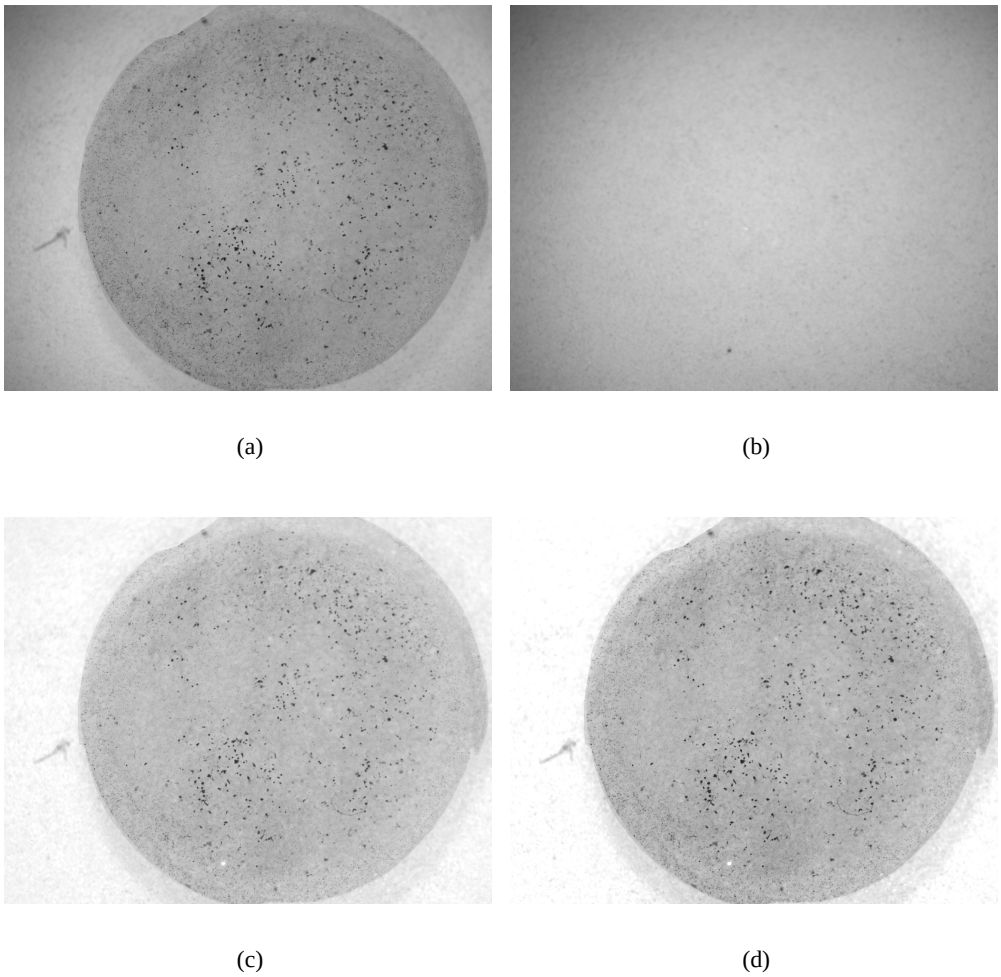

(a) (b)

(c) (d)

Figure 3.9: (a) An image of an *in vitro* invasion assay with nonuniform illumination. (b) An image of an empty slide under the same illumination. (c) The original image after correction of nonuniform illumination using the additive model. (d) The original image after correction of nonuniform illumination by the multiplicative model.

well as the image of an empty slide in Figure 3.9(b) show a clear vignetting effect. The result after correction of nonuniform illumination using Equation (2.9) is shown in Figure 3.9(c), and the result using Equation (2.10) is shown in Figure 3.9(d). The maximum value of the empty slide is used as the normalization coefficient in both cases, that is, $C_a = \max[\xi_a(m,n)]$ and $C_m = \max[\xi_m(m,n)]$. It can be seen that in both cases the vignetting effect has been removed and the circular well stands out appropriately from the rest of the image.

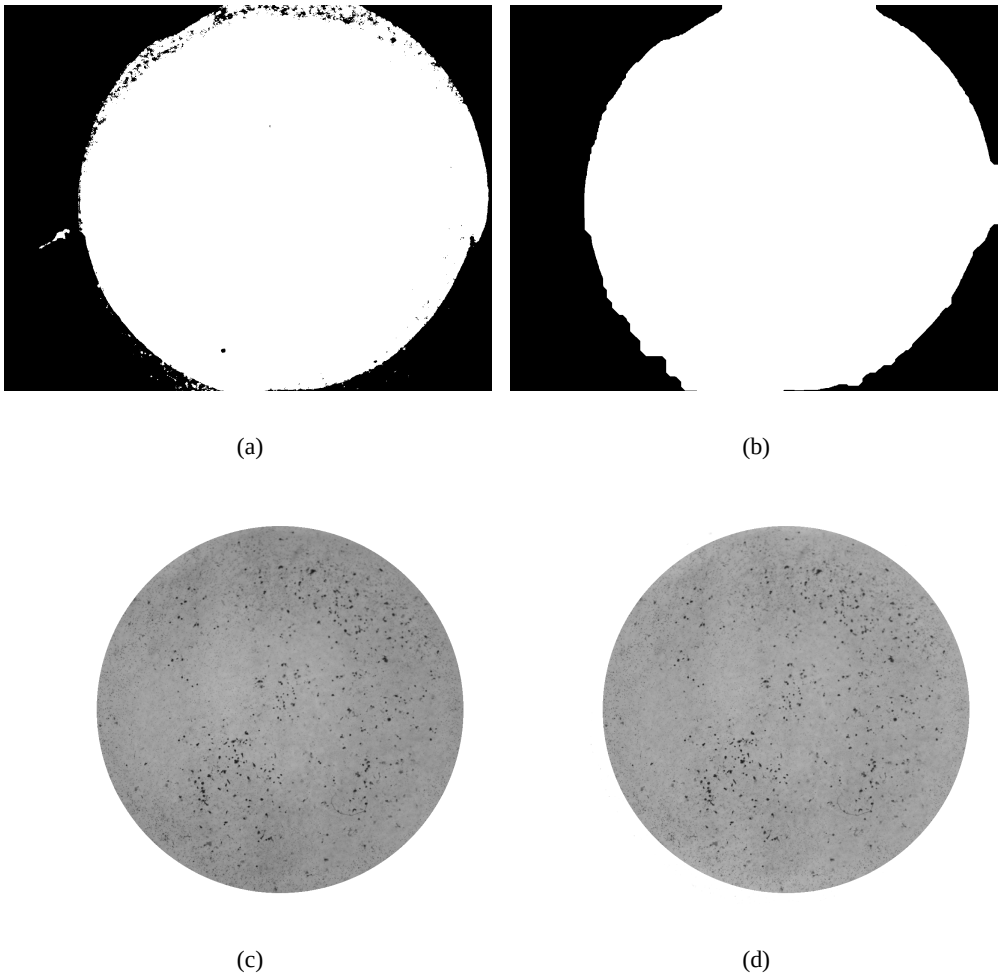

(a) (b)

(c) (d)

Figure 3.10: (a) Initial region of interest (ROI) detection with global thresholding. (b) The ROI mask after morphological filtering. (c) The circular fitted ROI. (d) The circular ROI after correction of nonuniform illumination.

The next pre-processing step is the detection of the region of interest (ROI), that is, the segmentation of the well from the background. An initial ROI detection is made with global thresholding using Otsu's method [75]. In the initial detection there may be some errors. For example, the detected ROI may have holes, correctly recognized ROI pixels may belong to more than one connected component, and pixels that do not belong to the ROI may be falsely recognized as ROI pixels. These problems are solved with a sequence of morphological filters. A circle is thereafter fitted on the detected ROI. Finally, correction of nonuniform illumination is performed anew, considering just the pixels within the detected region of interest. The additive model is again assumed, and

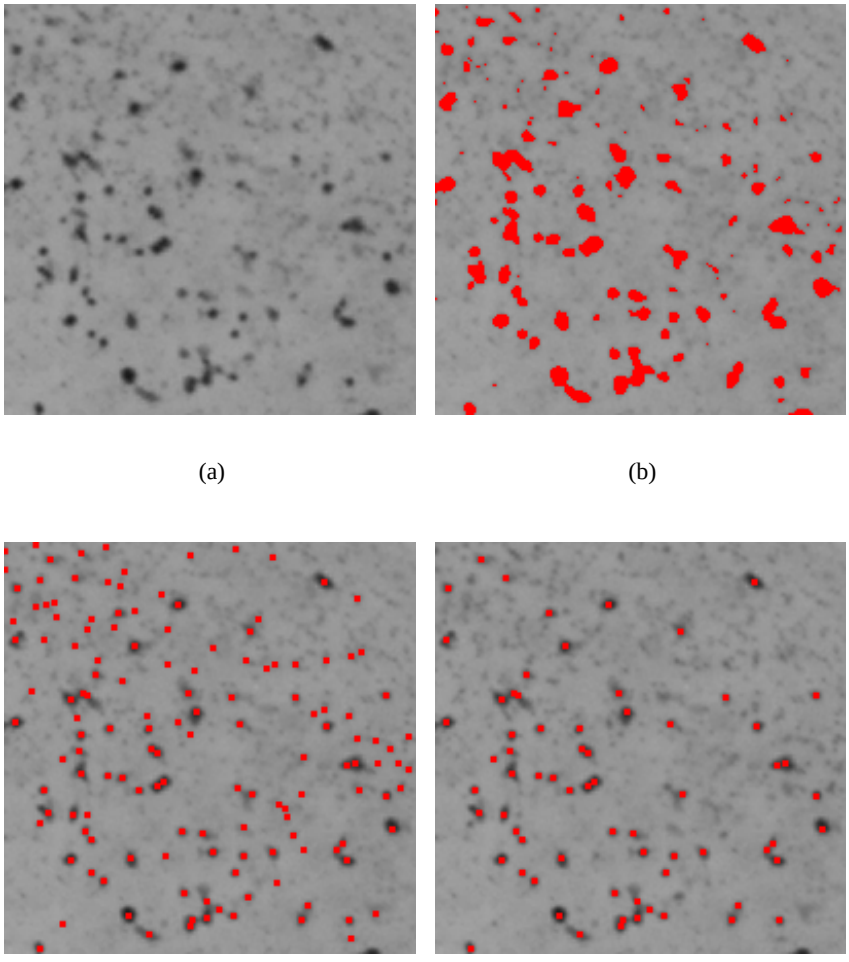

(a) (b)

(c) (d)

Figure 3.11: (a) A fraction of an image of an *in vitro* invasion assay. (b) Potential cell areas. (c) Potential cell locations. (d) Final cell detection result.

a second degree polynomial surface fit is used to estimate the nonuniformity component ξ_a. Figure 3.10 shows an example of ROI detection for the image shown in Figure 3.9.

3.2.3 Segmentation

In the invasion assay images cells are shown as dark points. The pores are also visible, but they are lighter and smaller than the cells. Figure 3.11(a) shows a 200×200 pixel fraction of the full image shown in Figure 3.9(a). Several cells as well as pores can be observed in this image.

The first step of the segmentation method is to make a crude detection of potential cell areas. This is done by global thresholding using Otsu's method [75]. The result for the example image is shown superimposed in red color on the original image in Figure 3.11(b). All pixels that represent an invaded cell have been correctly recognized. However, at the same time a lot of pixels that represent a pore or the background are recognized as well. Therefore, the segmentation result needs to be improved.

Because the aim is only to find the number of invaded cells and not their areas, we detect the darkest point of each invaded cell. Therefore, the second step of the segmentation method is to find the local minima within the detected potential cell areas. The result for the example image is shown in Figure 3.11(c). A 5×5 sliding window was used to find the local minima. Finally, the local minima are replaced by the local means using a small neighborhood, and these data points are divided into two classes using a threshold obtained with Otsu's method. The result for the example image is shown in Figure 3.11(d). A 3×3 local neighborhood was used to calculate the local means.

By using the local means of local minima, the segmentation method is able to distinguish between pores and invaded cells. Namely, the local mean depends on both the intensity and the size of the structure at which the local minimum is found. Note especially that even if the darkest pixels inside some pores are darker than the darkest pixels inside some of the invaded cells, the surrounding pixels are much lighter in the pores, which makes the mean intensity smaller. Moreover, the fact that the nuclei of the invaded cells are often seen as dark points within the cells makes it a good choice to use local minima as the location markers.

In the last step of the segmentation method it is also possible to use more features than just the local mean. For example, the local variance could be a good additional feature, because the local variance is high at the locations of the cells and lower in other locations. To be able to incorporate more features, thresholding the mean values is replaced by a clustering method (see Section 2.3.2). In [43] and in [87] such an approach with K-means clustering and fuzzy C-means clustering, respectively, is taken in very similar segmentation tasks.

3.2.4 Feature extraction

The segmentation method guarantees that there is exactly one foreground pixel for each detected cell. Therefore, the number of invaded cells is calculated by simply finding the sum of the pixel values in the binary segmentation result. However, since the area of the region of interest may be different for different images, the absolute amounts of invaded cells are not comparable between assays. Instead, the amount of invaded cells relative to the area of the ROI is recorded. For example, the number of cells per 100 pixels may be recorded.

3.2.5 Validation

Validation was done by comparing the counts obtained with the image analysis method with manual cell counts. The manual cell counts were done on the basis of digital images. The results show percent differences of less than 10 per cent. Moreover, there is a good correlation between the automated and manual counts: as far as comparing cell counts from different images is concerned, the automatic and manual results do not contradict each other. It should also be noted that the results obtained by manual counting may not be correct, and comparisons between the automated and manual counts are suggestive at best.

3.2.6 Data analysis

The image analysis method presented above was used in [59] to asses the role of increased insulin-like growth factor binding protein 2 (IGFBP2) in ovarian cancer cells. It was shown that IGFBP2 increases the invasion capacity of ovarian cancer cells. Since IGFBP2 is significantly over-expressed in invasive ovarian carcinomas as compared with normal ovarian tissues, blockage of IGFBP2 may constitute a viable strategy for targeted cancer therapy.

3.3 Quantification of buds and peroxisomes in budding yeast

Due to its relative simplicity, the budding yeast *Saccharomyces cerevisiae* is often used as a model organism. The sequence of *S. cerevisiae* was completed in 1996 [40]. By producing knockout strains it is possible to study the global regulation of different properties of yeast. For example, the regulation of yeast morphology was considered in [73, 84, 95] with the emphasis on developing an image analysis method for automated extraction of yeast cell morphology. Similar image analysis methods can also be used in cell cycle studies in which the aim is to invert the population effects [9, 68]. In [54] knockout mutants and image analysis methods were used to study endocytosis in budding yeast.

Publications IV and V propose image analysis methods for quantitative analysis of budding yeast. The main emphasis is in the segmentation of yeast cells and their buds. In Publication IV the motivation is to obtain information on the cell cycle phase of the population by quantifying bud sizes. Publication V presents a method that can be used to study peroxisome biogenesis in budding yeast.

3.3.1 Image acquisition

In the experiment used in Publication IV the cell population was synchronized using an alpha factor-based synchronization method [37]. Samples of the cultivated population were imaged using a bright field microscope using a resolution of 2776×2074 pixels and 8 bits per pixel and the sampling interval of 2 minutes. One of the images is shown

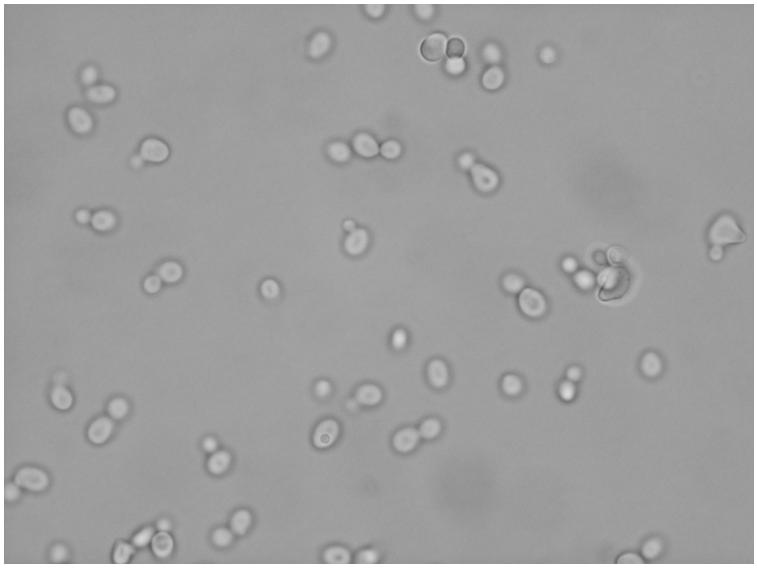

Figure 3.12: A bright fi eld image of a budding yeast *S. cerevisiae* population.

in Figure 3.12. In addition, samples taken with the sampling interval of 6 minutes were analyzed with a fluorescence-activated cell sorter (FACS). The imaging and FACS analysis were performed for a total of 280 minutes.

In the experiment used in Publication V a confocal microscope was used to obtain two images for each sample: a bright field image that visualizes the cells and a fluorescent counterpart that shows the peroxisomes marked with a green fluorescent protein (GFP). The resolution 512×512 pixels and 8 bits per pixel were used for both types of images. Figure 3.13 shows an example image pair.

3.3.2 Pre-processing

The first step is the correction of nonuniform illumination in the bright field images. The additive illumination model is assumed, and the nonuniformity component ξ_a is found with a separated second order polynomial fit, as described in Section 3.1.2.

The fluorescent images contain impulsive noise, which is removed with the 3×3 median filter. The result for the image in Figure 3.13(b) is shown in Figure 3.14.

3.3.3 Segmentation

In a bright field image of a yeast population, the cell membranes are clearly visible as elliptic regions that are darker than the background. The cell membrane pixels thus have two useful properties: the local mean is low and the local variance is high. Segmentation can be achieved by marking as cell membrane pixels those pixels whose local

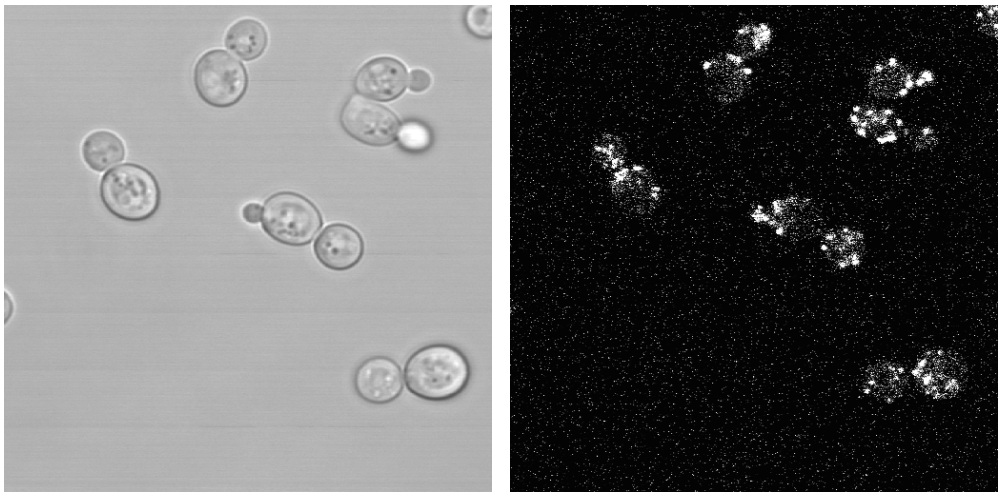

(a) (b)

Figure 3.13: A budding yeast *S. cerevisiae* population. (a) A bright field image showing the yeast cells. (b) A fluorescent image showing the peroxisomes marked with green fluorescent protein.

mean is below a threshold T_μ and whose variance is above a threshold T_σ. The threshold T_μ can be determined based on the global mean and variance of the local mean image. Similarly, the threshold T_σ can be determined based on the global mean and variance of the local variance image. Segmentation of the cell membranes is completed by filling the holes in the cell membranes and removing all small foreground objects by using morphological operations. Segmentation of the cells is thereafter completed by a simple flood fill of the areas inside the inner boundaries of the cell membranes.

In order to enable individual analysis of each cell and bud, the cells and buds must be separated from each other. The same applies also to cells that are clustered together. In Publication IV the separation method is based on two criteria [8]. The first one is a compactness measure

$$c = \frac{4\pi A}{p^2}, \tag{3.9}$$

where A is the area of an object and p is the length of its boundary line. Both quantities are measured in pixels, but note that c is a dimensionless quantity. Objects for which c is below a predefined threshold are candidates for objects that need to be split. The second criterion is

$$r = \max_{\mathbf{p}_1,\mathbf{p}_2 \in B} \frac{l_B(\mathbf{p}_1, \mathbf{p}_2)}{l_E(\mathbf{p}_1, \mathbf{p}_2)}, \tag{3.10}$$

where $\mathbf{p}_1 = (m_1, n_1)$ and $\mathbf{p}_2 = (m_2, n_2)$ are the coordinates of two points on the boundary of the object, B is the set of boundary coordinates, l_B is the distance between

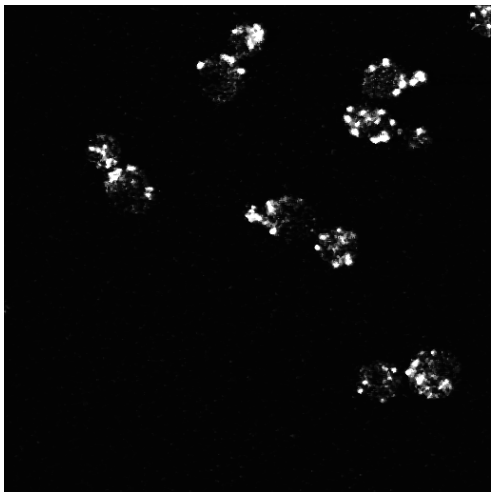

Figure 3.14: The fluorescent image shown in Figure 3.13(b) after filtering with the 3×3 median filter.

the points along the boundary of the object, and l_E is the Euclidean distance between the points. If r is above a predefined threshold, a splitting line is drawn between $\mathbf{p}_1$ and $\mathbf{p}_2$. The final segmentation result for the image shown in Figure 3.12 is shown in Figure 3.15.

In Publication V separation of clustered cells is done with a shape-based watershed separation method (see Section 2.3.5). The watershed transformation is applied to the Euclidean distance transformation [17] of the complement of the binary segmentation result. The h-maxima transformation is applied to avoid over-segmentation. The final segmentation result for the image shown in Figure 3.13(a) is shown in Figure 3.16(a). Peroxisomes are segmented from the fluorescent image by thresholding the median filtered image. In Publication V a constant threshold value 240 was used, because in the data peroxisome pixels are consistently very close to saturation. The watershed separation method is thereafter applied to the binary image in order to separate peroxisomes that are clustered together. The final segmentation result for the image shown in Figure 3.13(b) is shown in Figure 3.16(b).

3.3.4 Feature extraction

In Publication IV the area of each bud and the total number of cells are extracted. This allows us to determine the relative amounts of buds of different sizes in each image. These features can be readily extracted from the segmentation results. In Publication V the number of peroxisomes for each cell is determined. The detected cells in the bright field image are used as regions of interest for the peroxisomes in the respective fluorescent image.

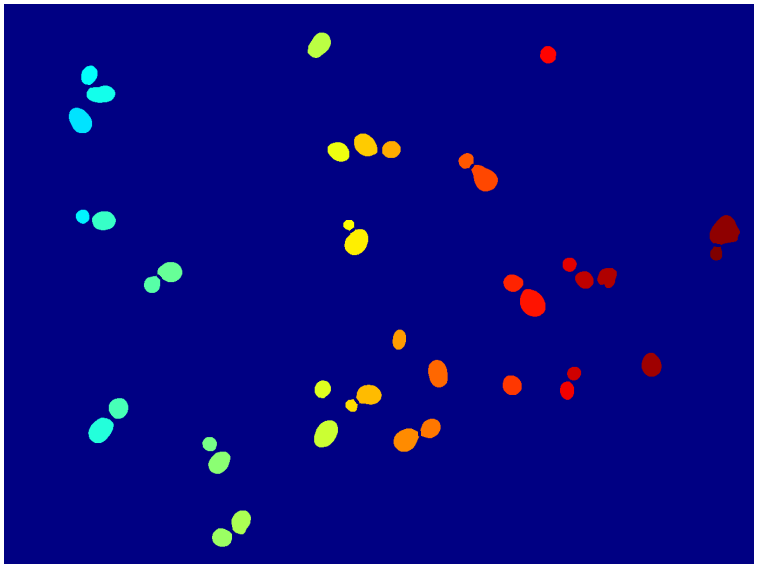

Figure 3.15: The final segmentation result for the image shown in Figure 3.12. Each cell and bud is shown with a different color. Cells that touch the edges of the image have been removed.

3.3.5 Validation

In [72] the estimates of the cell cycle distribution obtained with the image analysis method presented in Publication IV were compared with distribution estimates obtained with a method based on FACS measurements. The obtained distributions are in agreement with each other, which suggests that the image analysis method gives valid results.

The image analysis method presented in Publication V was tested with 25 test image pairs taken of the same yeast strain. The automatically obtained number of cells in each image was compared with manual cell counts. The results are illustrated as a scatter plot in Figure 3.17(a). In most cases the automated counts given by the presented image analysis method differ from the manual counts by at most one cell. More significant inaccuracies occur only when there is a large number of cells in the image. In those cases large numbers of cells are clustered together, and the watershed method is unable to separate them all.

Because of the large amount of noise in the fluorescent images, the manual counting of the numbers of peroxisomes in the cells is difficult and tedious. However, the manual counts were obtained for 30 randomly selected cells. The results are illustrated as a scatter plot in Figure 3.17(b). It can be seen that the automated counts are very close to the manual counts. However, it should be emphasized that the manual counts may contain errors. In fact, it may even be the case that the manual count for a given cell is incorrect and the automated count is correct. The automated method seems to have a tendency to produce higher peroxisome counts than manual counting.

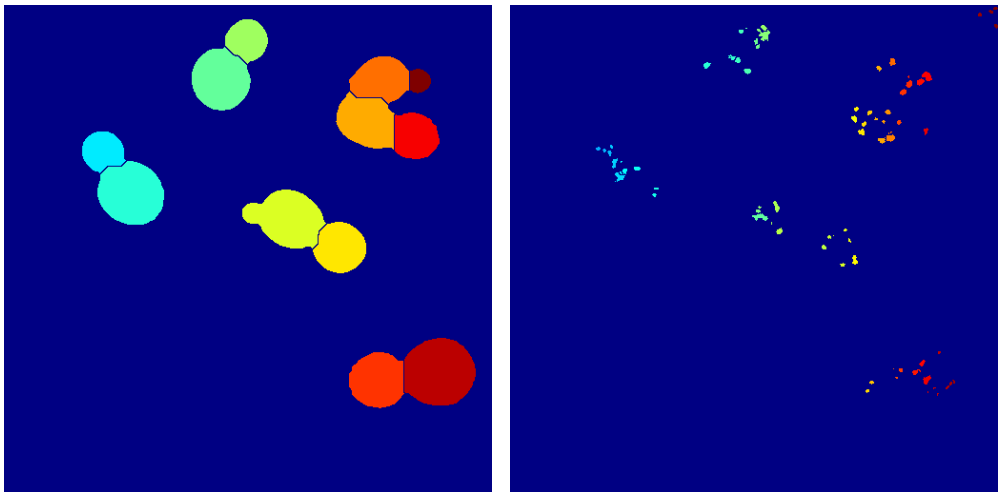

(a) (b)

Figure 3.16: (a) The final segmentation result for the image shown in Figure 3.13(a). Each cell is shown with a different color. Cells that touch the edges of the image have been removed. (b) The final segmentation result for the image shown in Figure 3.13(b). Each peroxisome is shown with a different color.

3.3.6 Data analysis

Inversion of population effects

The gene expression levels of cell cycle regulated genes are often observed as a time series. Because the cell population is in practice never perfectly synchronized, that is, all cells are not in the same phase of the cell cycle, the measured gene expression level is a convolution of true values from neighboring cell cycle phases. The principles of the inversion of this population effect are described in [68]. One of the described methods uses bud counting data obtained with an image analysis method such as the one presented in Publication IV.

Peroxisome biogenesis

The method presented in Publication V can be used to relate different gene knockouts to peroxisome biogenesis. As a simple example, deletion of genes involved in the biogenesis of peroxisomes would show a paucity of peroxisomes. Thus, if a gene whose effect is unknown is deleted and a paucity of peroxisomes is observed with the image analysis method, it may be concluded that the gene is involved in peroxisome biogenesis.

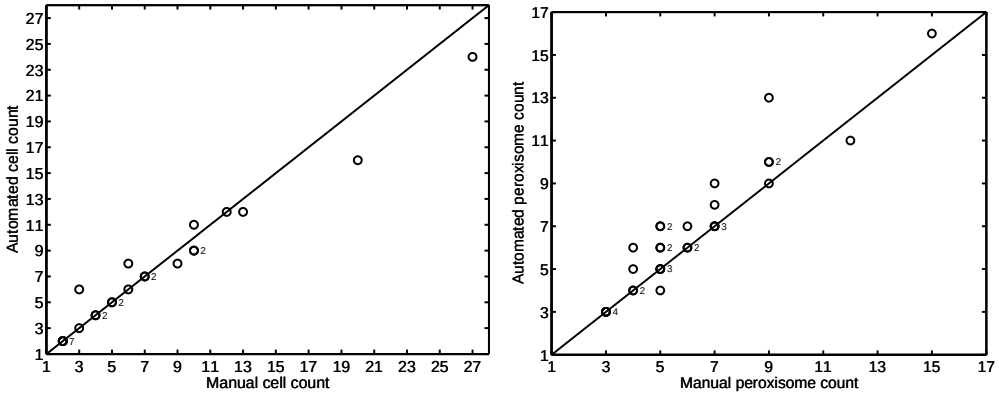

(a) (b)

Figure 3.17: (a) The scatter plot of manual cell counts vs. automated cell counts for 25 test images. (b) The scatter plot of manual peroxisome counts vs. automated peroxisome counts for 30 cells.

3.4 Quantification of lymph node size and number

Colorectal cancer is one of the most common types of cancer. The American Cancer Society estimates that in the United States in the year 2006 about 148610 people will be diagnosed with colorectal cancer and that over 55170 people will die of the disease [3]. It can be estimated that at least 30000 of the diagnosed cases of colorectal cancer will be stage II and that several thousand of the stage II patients will eventually die of the disease [109].

Some patients diagnosed with stage II colorectal cancer may benefit from adjuvant chemotherapy. Because of the adverse effects of chemotherapy, the selection of patients who are given this additional treatment must be done carefully so that chemotherapy is given to only those patients that will benefit from it. The image analysis method presented in Publication VI gives a solution for extracting two important prognostic markers: the numbers and sizes of the lymph nodes recovered in surgical specimens of colorectal cancer.

3.4.1 Image acquisition

The histopathologic sections of lymph nodes of 150 consecutive patients with stage II colorectal cancer at The University of Texas M. D. Anderson Cancer Center between 1990 and 1998 were imaged with a standard desktop image scanner using the scanning resolution 300 dpi. The histopathologic sections had been stained with the H&E stain and put on slides at the time they had been recovered in surgery. Hematoxylin binds to the lymph nodes and eosin is mainly washed away. Each slide can contain multiple

lymph nodes and each image can contain multiple slides. There were 1069 slides in total.

3.4.2 Pre-processing

The first task is to recognize the slides from each image. An example of a scanned image with 7 slides is shown in Figure 3.18(a). The edges of the slides result in shadows that can be seen as dark lines between the slides. These lines are detected with the aid of a vertical projection of the image in a way akin to projection-based methods for gridding of microarrays, see, for example, [5, 49].

3.4.3 Segmentation

The detection of lymph nodes is done slide by slide. The initial detection is done with K-means clustering in the CIE L*a*b* color space. Three clusters are used. One of the clusters corresponds to the the dark blue lymph nodes, one to the white background, and one to the light pink structures that are not lymph nodes. The K-means clustering result for the slides shown in Figure 3.18(a) is shown in Figure 3.18(b). It is then straightforward to obtain a binary image that represents the lymph nodes by simply replacing the values that represent the appropriate cluster by the foreground label and the values that represent the other two cluster by the background label. Finally, a sequence of morphological operations is applied. The result for the slides shown in Figure 3.18(a) is shown in Figure 3.18(c).

3.4.4 Feature extraction

The number of lymph nodes in each slide can be detected simply by finding the number of connected components. The area of the lymph nodes can be found by calculating the number of pixels in each connected component. A conversion into metric units is possible because we know the resolution of the scanner. The area of the cross section of the lymph nodes is used as a measure of the size of the lymph node. The area naturally depends on how the histopathologic section of the lymph node was cut when it was recovered by the pathologist. However, in this study it is enough to obtain rough measurements of lymph node size.

3.4.5 Validation

The number of lymph nodes found in each surgical specimen was recorded by the pathologists when the lymph nodes were originally recovered. We compared these manual counts with the counts obtained with our automated image analysis method. The scatter plot of the comparison is shown in Figure 3.19. The observations fit well onto a straight line, and it can be concluded that the lymph node counts given by our automated image analysis method are accurate.

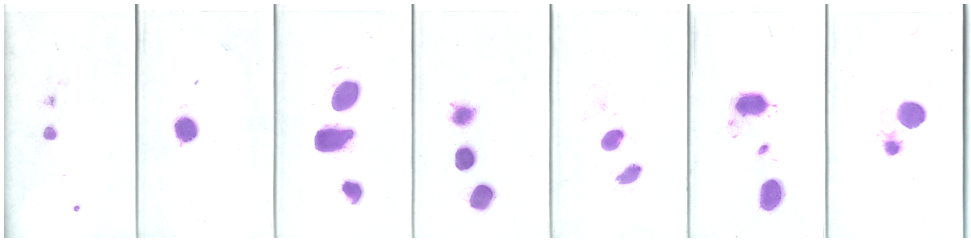

(a)

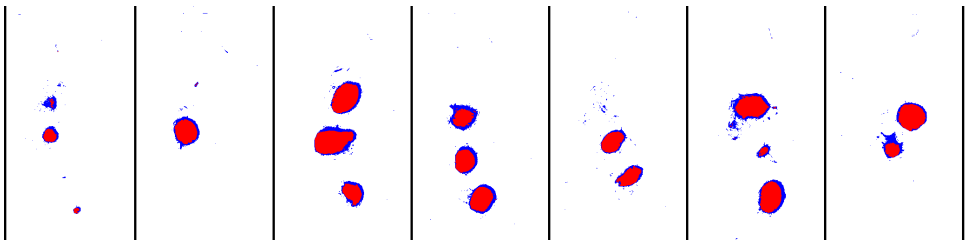

(b)

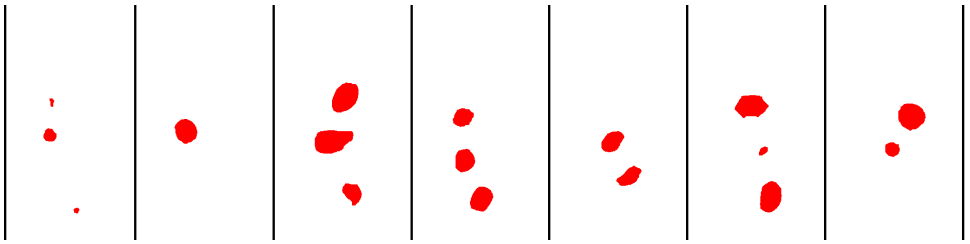

(c)

Figure 3.18: (a) An image with 7 lymph node slides. (b) The K-means clustering result with lymph nodes marked red. (c) The final segmentation result with lymph nodes marked red.

3.4.6 Data analysis

The image analysis method presented in Publication VI was used in [22, 23] to show that the size and number of lymph nodes can be used to predict survival in colorectal cancer. As in previous reports, a larger number of examined lymph nodes was associated with better overall survival: median survival was 127 ± 5.75 (standard error) months for patients with more than eleven lymph nodes as contrasted with 105 ± 7.21 months. In addition, the median overall survival of patients with larger lymph nodes

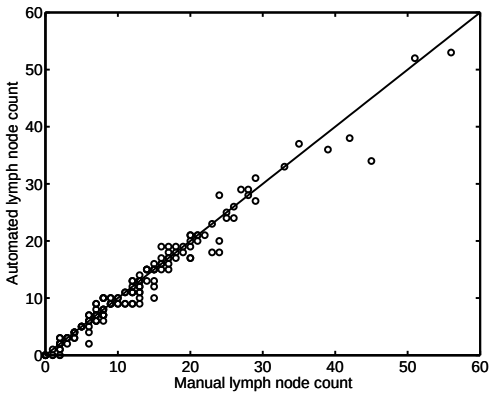

Figure 3.19: Correlation of manual and automated lymph node counts.

was longer: 127 ± 5.85 months vs. 105 ± 7.03 months. The sum of the sizes of the nodes was a significant predictor for survival. Overall survival was best in patients with large numbers of large nodes and worst in those with small numbers of small nodes. In multivariate analysis, overall survival was independently predicted by the size of negative lymph nodes.

Chapter 4

Discussion

The field of this thesis is in constant development. On the one hand, studies that utilize automated image analysis are published in biological journals with an increasing frequency. On the other hand, research on image analysis methods is very active. It is clear that at this point final solutions to the general image analysis problem cannot be offered. However, the field is rapidly moving forward in small increments.

Many of the challenges in image analysis are of a fundamental nature. For example, in image segmentation the crucial question is how well the segmentation method generalizes for new images that have not been seen during the development of the method. In thresholding it is assumed that all foreground pixels are separated by intensity from all background pixels. If this simple model holds for the new images, they can be segmented correctly by thresholding. However, the appropriate model may be more complicated. For example, edge intensities or shape information may be required to describe the foreground objects. By making the model more complicated it is in principle possible to develop a segmentation method that performs perfectly for all the images that are available. However, then the problem is that the method may be over-fitted to the available images so that new images that will be encountered are segmented incorrectly. The problem is exactly the same as in supervised classification: generalization should be ensured by avoiding over-fitting to the training data.

Automated image analysis combined with data analysis techniques seems to offer a lot of new possibilities in biology. The biggest challenge seems to be in finding ways in which scientists coming from different disciplines can work together. The mere identification of the situations where automated image analysis can be useful may at times be difficult. One of the considerations is how much the image analysis method can be controlled by the user. For example, if a high-throughput system capable of analyzing thousands of images in a reasonable time is required, the system must most likely be fully automated. If the amount of image data is smaller but the problem is too difficult to be analyzed manually, an automated method in which the user has access to some of the parameters may be more appropriate. Usually these decisions cannot be made by a biologists or an engineer alone, and it is required that both have a reasonable

understanding of both the biological and the technical dimensions of the problem. It is certain that the most exciting results can be reached when biologists, medical doctors, engineers, mathematicians, and statisticians work together towards a common goal.

Chapter 5

Comments on publications

This thesis consists of seven publications. No other dissertation is based on any of the publications. The work started at the Institute of Signal Processing, Tampere University of Technology, in 2002. Publications I, II, III, and VI resulted from the author's research visit to The University of Texas M. D. Anderson Cancer Center in Houston, Texas, USA between September 2003 and March 2004. The author finished the manuscript of Publication V at the Institute for Systems Biology in Seattle, Washington, USA.

5.1 Author's contribution to publications

The author of this thesis is the first author of all seven publications. The author has therefore been responsible for the overall manuscript preparation, including integration of the biological and technical parts of the articles. Most of the image analysis methods presented in the publications have been developed or implemented by the author and the biological wet lab experiments were mainly carried out by the co-authors.

In Publication I the image analysis method was developed by the author. The validation of the results by testing positive, negative, and no treatment controls as well as the robustness analysis was also done by the author. In Publication II the author designed the comparison of the invasion percolation (IP) and diffusion limited aggregation (DLA) growth models, including the selection of the particular type of IP and DLA models and the parameter values. The author also implemented the DLA model and made the tests that established the power law behavior of experimental angiogenesis data.

The image analysis method of Publication III was developed by the author. The author also performed the validation of the results.

In Publications IV and V the author was responsible for the image analysis methods with the exception of the mean-variance segmentation method and the watershed separation method. The author also helped to perform the wet lab experiment for Publication IV and made the analysis for validation of the results in Publication V.

In Publication VI the author was responsible for the image analysis method and its validation with the help of the data produced by the pathologists who had recovered the lymph nodes between 1990 and 1998.

In Publication VII the author was responsible for the development of the misclassification correction method based on an initial version developed by the co-authors and published in 1999. The author also developed the training-based approach for learning the proximity function and made the simulations as well as the assessment of accuracy.

5.2 Errata

In addition to some misprints, the following errors have been found in the publications.

- In Publication I the condition for i in the first sentence of the second paragraph of Section II-A should be $i \in [1, n-1]$.
- In Publication I one of the quantified parameters is referred to as the tubule complex size. However, it would be more appropriate to refer to tubule complex area.
- In Publication II the journal of Reference 11 should be *Mathematical Medicine and Biology*.
- In Publication III the segmentation result in Figure 5(d) is incorrect. The correct segmentation result is presented in Figure 3.11(d) of this thesis.
- In Publication IV one of the quantified parameters is referred to as the bud size. However, it would be more appropriate to refer to bud area.
- In Publication VI the number of patients is cited incorrectly as 148 in the last paragraph of Section I and in the first paragraph of Section II. The correct number of patients is 150.

Bibliography

[1] B. Alberts, D. Bray, J. Lewis, M. Raff, K. Roberts, and J. D. Watson, *Molecular Biology of the Cell*, 3rd ed. New York: Garland Publishing, 1994.

[2] A. Albini, Y. Iwamoto, H. K. Kleinman, G. R. Martin, S. A. Aaronson, J. M. Kozlowski, and R. N. McEwan, "A rapid *in vitro* assay for quantitating the invasive potential of tumor cells," *Cancer Research*, vol. 47, no. 12, pp. 3239–3245, June 1987.

[3] American Cancer Society, "Cancer facts and figures 2006," ACS Publications, Atlanta, Georgia, 2006.

[4] M. Anderson, R. Motta, S. Chandrasekar, and M. Stokes, "Proposal for a standard default color space for the internet: sRGB," in *Proceedings of the IS&T/SID 4th Color Imaging Conference: Color Science, Systems and Applications (CIC'96)*, Scottsdale, Arizona, USA, November 19–22, 1996, pp. 238–246.

[5] J. Angulo and J. Serra, "Automatic analysis of DNA microarray images using mathematical morphology," *Bioinformatics*, vol. 19, no. 5, pp. 553–562, March 2003.

[6] F. Arnold and D. C. West, "Angiogenesis in wound healing," *Pharmacology & Therapeutics*, vol. 52, no. 3, pp. 407–422, December 1991.

[7] J. Astola and P. Kuosmanen, *Fundamentals of Nonlinear Digital Filtering*. Boca Raton, Florida: CRC Press, 1997.

[8] D. Balthasar, T. Erdmann, J. Pellenz, V. Rehrmann, J. Zeppen, and L. Priese, "Real-time detection of arbitrary objects in alternating industrial environments," in *Proceedings of the 12th Scandinavian Conference on Image Analysis (SCIA'01)*, Bergen, Norway, June 11–14, 2001, pp. 321–328.

[9] Z. Bar-Joseph, S. Farkash, D. K. Gifford, I. Simon, and R. Rosenfeld, "Deconvolving cell cycle expression data with complementary information," *Bioinformatics*, vol. 20, no. Supplement 1, pp. i23–i30, August 2004.

[10] A.-L. Barabási and R. Albert, "Emergence of scaling in random networks," *Science*, vol. 286, no. 5439, pp. 509–512, October 1999.

[11] E. Bengtson, O. Erikson, J. Holmquist, T. Jarkrans, B. Nordin, and B. Stenkvist, "Segmentation of cervical cells: detection of overlapping cell nuclei," *Computer Graphics and Image Processing*, vol. 16, no. 4, pp. 382–394, August 1981.

[12] S. Beucher and C. Lantuéjoul, "Use of watersheds in contour detection," in *Proceedings of the International Workshop on Image Processing: Real-Time and Motion Detection/Estimation*, Rennes, France, September 17–21, 1979.

[13] J. C. Bezdek, *Pattern recognition with fuzzy objective function algorithms*. New York: Plenum Press, 1981.

[14] E. T. Bishop, G. T. Bell, S. Bloor, I. J. Broom, N. F. K. Hendry, and D. N. Wheatley, "An *in vitro* model of angiogenesis: basic features," *Angiogenesis*, vol. 3, no. 4, pp. 335–344, July 1999.

[15] R. J. Blatt, A. N. Clark, J. Courtney, C. Tully, and A. L. Tucker, "Automated quantitative analysis of angiogenesis in the rat aorta model using Image-Pro Plus 4.1," *Computer Methods and Programs in Biomedicine*, vol. 75, no. 1, pp. 75–79, July 2004.

[16] A. Bleau and L. J. Leon, "Watershed-based segmentation and region merging," *Computer Vision and Image Understanding*, vol. 77, no. 3, pp. 317–370, March 2000.

[17] G. Borgefors, "Distance transformations in digital images," *Computer Vision, Graphics, and Image Processing*, vol. 34, no. 3, pp. 344–371, June 1986.

[18] J. F. Canny, "A computational approach to edge detection," *IEEE Transactions on Pattern Analysis and Machine Intelligence*, vol. 8, no. 6, pp. 679–698, November 1986.

[19] M. A. J. Chaplain, "Mathematical modelling of angiogenesis," *Journal of Neuro-Oncology*, vol. 50, no. 1-2, pp. 37–51, October–November 2000.

[20] Y.-S. Chen and Y.-T. Yu, "Thinning approach for noisy digital patterns," *Pattern Recognition*, vol. 29, no. 11, pp. 1847–1862, November 1996.

[21] Z. Chen and S. Molloi, "Multiresolution vessel tracking in angiographic images using valley courses," *Optical Engineering*, vol. 42, no. 6, pp. 1673–1682, June 2003.

[22] L. R. Chirieac, Y. Suehiro, A. Niemistö, I. Shmulevich, S. Lunagomez, J. Morris, and S. R. Hamilton, "Size and number of examined lymph nodes impacts outcome in patients with stage II colorectal cancer," *Journal of Clinical Oncology*, 2004 ASCO Annual Meeting Proceedings, vol. 22, no. 14S, July 2004.

[23] ——, "Size and number of negative lymph nodes impact outcome in patients with node-negative stage II colorectal cancer," in *2005 Annual Meeting of the United States and Canadian Academy of Pathology (USCAP'05)*, San Antonio, Texas, USA, February 26 – March 4, 2005.

[24] Commission Internationale de l'Éclairage (CIE), "Recommendations on uniform color spaces, color-difference equations, and psychometric color terms," CIE publication no. 15, supplement 2, Paris, France, 1976.

[25] A. Condurache and T. Aach, "Vessel segmentation in angiograms using hysteresis thresholding," in *Proceedings of the 9th IAPR Conference on Machine Vision Applications (MVA'05)*, Tsukuba Science City, Japan, May 16–18, 2005, pp. 269–272.

[26] J. C. Cross, Z. Werb, and S. J. Fisher, "Implantation and the placenta: key pieces of the development puzzle," *Science*, vol. 266, no. 5190, pp. 1508–1518, December 1994.

[27] H. Digabel and C. Lantéujoul, "Iterative algorithms," in *Proceedings of the 2nd European Symposium on Quantitative Analysis of Microstructures in Material Science, Biology and Medicine*, Caen, France, October 1977, J. L. Chermant, Ed. Stuttgart, Germany: Riederer Verlag, 1978, pp. 85–89.

[28] C. N. Doukas, I. Maglogiannis, A. Chatziioannou, and A. Papapetropoulos, "Automated angiogenesis quantification through advanced image processing techniques," in *Proceedings of the 28th Annual International Conference of the IEEE Engineering in Medicine and Biology Society (EMBC'06)*, New York, USA, August 30 – September 3, 2006, pp. 2345–2348.

[29] W. Doyle, "Operations useful for similarity-invariant pattern recognition," *Journal of the ACM*, vol. 9, no. 2, pp. 259–267, April 1962.

[30] R. O. Duda, P. E. Hart, and D. G. Stork, *Pattern Classification*, 2nd ed. New York: Wiley, 2001.

[31] V. Dunmire, A. Niemistö, I. Shmulevich, and W. Zhang, "Effects of insulin-like growth factor-binding proteins 1 through 5 on *in vitro* angiogenesis assay," in *Proceedings of the American Association for Cancer Research (AACR'04)*, Orlando, Florida, USA, March 27–31, 2004, p. 1002.

[32] J. C. Dunn, "A fuzzy relative of the ISODATA process and its use in detecting compact well-separated clusters," *Journal of Cybernetics*, vol. 3, no. 3, pp. 32–57, 1973.

[33] N. Ferrara and K. Alitalo, "Clinical applications of angiogenic growth factors and their inhibitors," *Nature Medicine*, vol. 5, no. 12, pp. 1359–1364, December 1999.

[34] N. Ferrara and R. S. Kerbel, "Angiogenesis as a therapeutic target," *Nature*, vol. 438, no. 7070, pp. 967–974, December 2005.

[35] J. Folkman, "Role of angiogenesis in tumor growth and metastasis," *Seminars in Oncology*, vol. 29, no. 6, pp. 15–18, December 2002.

[36] J. R. Fram and E. S. Deutsch, "On the quantitative evaluation of edge detection schemes and their comparison with human performance," *IEEE Transactions on Computers*, vol. 24, no. 6, pp. 616–628, June 1975.

[37] B. Futcher, "Cell cycle synchronization," *Methods in Cell Science*, vol. 21, no. 2-3, pp. 79–86, June 1999.

[38] A. Gagliardi, H. Hadd, and D. C. Collins, "Inhibition of angiogenesis by suramin," *Cancer Research*, vol. 52, no. 18, pp. 5073–5075, September 1992.

[39] C. A. Glasbey, "An analysis of histogram-based thresholding algorithms," *CVGIP: Graphical Models and Image Processing*, vol. 55, no. 6, pp. 532–537, November 1993.

[40] A. Goffeau, B. G. Barrell, R. W. D. H. Bussey, B. Dujon, H. Feldmann, F. Galibert, C. J. J. D. Hoheisel, M. Johnston, E. J. Louis, H. W. Mewes, Y. Murakami, P. Philippsen, H. Tettelin, and S. G. Oliver, "Life with 6000 genes," *Science*, vol. 274, no. 5287, pp. 563–567, October 1996.

[41] R. C. Gonzalez and R. E. Woods, *Digital Image Processing*, 2nd ed. Upper Saddle River, New Jersey: Prentice Hall, 2002.

[42] E. Grisan, A. Pesce, A. Giani, M. Foracchia, and A. Ruggeri, "A new tracking system for the robust extraction of retinal vessel structure," in *Proceedings of the 26th Annual International Conference of the IEEE Engineering in Medicine and Biology Society (EMBC'04)*, San Francisco, California, USA, September 1–5, 2004, pp. 1620–1623.

[43] C. Gunduz, B. Yener, and S. H. Gultekin, "The cell graphs of cancer," *Bioinformatics*, vol. 20, no. Supplement 1, pp. i145–i151, August 2004.

[44] Z. Guo and R. W. Hall, "Parallel thinning with two-subiteration algorithms," *Communications of the ACM*, vol. 32, no. 3, pp. 359–373, March 1989.

[45] F. R. Hampel, E. M. Ronchetti, P. J. Rousseeuw, and W. A. Stahel, *Robust Statistics: The Approach Based on Influence Functions*. New York: Wiley, 1986.

[46] K. Haris, S. N. Efstratiadis, N. Maglaveras, and A. K. Katsaggelos, "Hybrid image segmentation using watersheds and fast region merging," *IEEE Transactions on Image Processing*, vol. 7, no. 12, pp. 1684–1699, December 1998.

[47] J. A. Hartigan and M. A. Wong, "A *k*-means clustering algorithm," *Applied Statistics*, vol. 28, no. 1, pp. 100–108, 1979.

[48] S. E. Hernandez, K. E. Barner, and Y. Yuan, "Region merging using homogeneity and edge integrity for watershed-based image segmentation," *Optical Engineering*, vol. 44, no. 1, January 2005.

[49] R. Hirata, Jr., J. Barrera, R. F. Hashimoto, D. O. Dantas, and G. H. Esteves, "Segmentation of microarray images by mathematical morphology," *Real-Time Imaging*, vol. 8, no. 6, pp. 491–505, December 2002.

[50] A. Hoover and M. Goldbaum, "Locating the optic nerve in a retinal image using the fuzzy convergence of the blood vessels," *IEEE Transactions on Medical Imaging*, vol. 22, no. 8, pp. 951–958, August 2003.

[51] K. Huang and R. F. Murphy, "From quantitative microscopy to automated image understanding," *Journal of Biomedical Optics*, vol. 9, no. 5, pp. 893–912, September/October 2004.

[52] International Telecommunications Union (ITU), "Studio encoding parameters of digital television for standard 4:3 and wide-screen 16:9 aspect ratios," Recommendation ITU-R BT.601-5, Geneva, Switzerland, 1995.

[53] A. K. Jain, M. N. Murty, and P. J. Flynn, "Data clustering: a review," *ACM Computing Surveys*, vol. 31, no. 3, pp. 264–323, September 1999.

[54] M. Kaksonen, C. P. Toret, and D. G. Drubin, "A modular design for the clathrin- and actin-mediated endocytosis machinery," *Cell*, vol. 123, no. 2, pp. 305–230, October 2005.

[55] R. Kerbel and J. Folkman, "Clinical translation of angiogenesis inhibitors," *Nature Reviews Cancer*, vol. 2, no. 10, pp. 727–739, October 2002.

[56] R. J. Kohler and H. K. Howell, "Photographic image enhancement by superposition of multiple images," *Photographic Science and Engineering*, vol. 7, no. 4, pp. 241–245, July – August 1963.

[57] T. Krecicki, D. Dus, J. Kozlak, W. Tarnawski, M. Jelen, M. Zalesska-Krecicka, and T. Szkudlarek, "Quantitative evaluation of angiogenesis in laryngeal cancer by digital image measurement of the vessel density," *Auris Nasus Larynx*, vol. 29, no. 3, pp. 271–276, July 2002.

[58] L. Lam, S.-W. Lee, and C. Y. Suen, "Thinning methodologies–a comprehensive survey," *IEEE Transactions on Pattern Analysis and Machine Intelligence*, vol. 14, no. 9, pp. 869–885, September 1992.

[59] E.-J. Lee, C. Mircean, I. Shmulevich, H. Wang, J. Liu, A. Niemistö, J. J. Kavanagh, J.-H. Lee, and W. Zhang, "Insulin-like growth factor binding protein 2 promotes ovarian cancer cell invasion," *Molecular Cancer*, vol. 4, no. 7, February 2005.

[60] A. Lehmussola, J. Selinummi, P. Ruusuvuori, A. Niemistö, and O. Yli-Harja, "Simulating fluorescent microscope images of cell populations," in *Proceedings of the 27th Annual International Conference of the IEEE Engineering in Medicine and Biology Society (EMBC'05)*, Shanghai, China, September 1–4, 2005, pp. 3153–3156.

[61] F. J. W.-M. Leong, M. Brady, and J. O. McGee, "Correction of uneven illumination (vignetting) in digital microscopy images," *Journal of Clinical Pathology*, vol. 56, pp. 619–621, 2003.

[62] T. Lillesand and R. Kiefer, *Remote Sensing and Image Interpretation*. New York: Wiley, 1994.

[63] G. Lin, U. Adiga, K. Olson, J. F. Guzowski, C. A. Barnes, and B. Roysam, "A hybrid 3D watershed algorithm incorporating gradient cues and object models for automatic segmentation of nuclei in confocal image stacks," *Cytometry Part A*, vol. 56A, no. 1, pp. 23–36, November 2003.

[64] J. Lindblad and E. Bengtsson, "A comparison of methods for estimation of intensity nonuniformities in 2D and 3D microscope images of fluorescence stained cells," in *Proceedings of the 12th Scandinavian Conference on Image Analysis (SCIA'01)*, Bergen, Norway, June 11–14, 2001, pp. 264–271.

[65] J. Lindblad, C. Wählby, E. Bengtsson, and A. Zaltsman, "Image analysis for automatic segmentation of cytoplasms and classification of Rac1 activation," *Cytometry Part A*, vol. 57A, no. 1, pp. 22–23, January 2004.

[66] H. Lodish, A. Berk, S. L. Zipursky, P. Matsudaira, D. Baltimore, and J. E. Darnell, *Molecular Cell Biology*, 4th ed. New York: Freeman, 2001.

[67] S. Y. Lu and K. S. Fu, "A sentence-to-sentence clustering procedure for pattern analysis," *IEEE Transactions on Systems, Man, and Cybernetics*, vol. 8, no. 5, pp. 381–389, May 1978.

[68] H. Lähdesmäki, T. Aho, H. Huttunen, M.-L. Linne, J. Niemi, J. Kesseli, R. Pearson, and O. Yli-Harja, "Estimation and inversion of the effects of cell population asynchrony in gene expression time-series," *Signal Processing*, vol. 83, no. 4, pp. 835–858, April 2003.

[69] J. B. MacQueen, "Some methods for classification and analysis of multivariate observations," in *Proceedings of the 5th Berkeley Symposium on Mathematical Statistics and Probability*, vol. 1, Berkeley, California, USA, 1967, pp. 281–297.

[70] N. Malpica, C. O. de Solórzano, J. J. Vaquero, A. Santos, I. Vallcorba, J. M. García-Sagredo, and F. del Pozo, "Applying watershed algorithms to the segmentation of clustered nuclei," *Cytometry*, vol. 28, no. 4, pp. 289–297, August 1997.

[71] F. Nekka, S. Kyriacos, C. Kerrigan, and L. Cartilier, "A model of growing vascular structures," *Bulletin of Mathematical Biology*, vol. 58, no. 3, pp. 409–424, May 1996.

[72] A. Niemistö, M. Nykter, T. Aho, H. Jalovaara, K. Marjanen, M. Ahdesmäki, P. Ruusuvuori, M. Tiainen, M.-L. Linne, and O. Yli-Harja, "Distribution estimation of synchronized budding yeast population," in *Proceedings of the Winter International Symposium on Information and Communication Technologies 2004 (WISICT'04)*, Cancun, Mexico, January 5–8, 2004, pp. 243–248.

[73] M. Ohtani, A. Saka, F. Sano, Y. Ohya, and S. Morishita, "Development of image processing program for yeast cell morphology," *Journal of Bioinformatics and Computational Biology*, vol. 1, no. 4, pp. 695–709, January 2004.

[74] L. Olsen, J. A. Sherratt, P. K. Maini, and F. Arnold, "A mathematical model for the capillary endothelial cell-extracellular matrix interactions in wound-healing angiogenesis," *IMA Journal of Mathematics Applied in Medicine and Biology*, vol. 14, no. 4, pp. 261–281, December 1997.

[75] N. Otsu, "A threshold selection method from gray-level histograms," *IEEE Transactions on Systems, Man, and Cybernetics*, vol. 9, no. 1, pp. 62–66, January 1979.

[76] M. J. Plank and B. D. Sleeman, "A reinforced random walk model of tumour angiogenesis and anti-angiogenic strategies," *Mathematical Medicine and Biology*, vol. 20, no. 2, pp. 135–181, June 2003.

[77] J. M. S. Prewitt and M. L. Mendelsohn, "The analysis of cell images," *Annals of the New York Academy of Sciences*, vol. 128, pp. 1035–1053, January 1966.

[78] L. A. Repesh, "A new *in vitro* assay for quantitating tumor cell invasion," *Invasion Metastasis*, vol. 9, no. 3, pp. 192–208, 1989.

[79] W. Risau, "Mechanisms of angiogenesis," *Nature*, vol. 386, no. 6626, pp. 671–674, April 1997.

[80] K. Rodenacker and E. Bengtsson, "A feature set for cytometry on digitized microscopic images," *Analytical Cellular Pathology*, vol. 25, no. 1, pp. 1–36, 2003.

[81] A. Rosenfeld and J. L. Pfaltz, "Sequential operations in digital picture processing," *Journal of the ACM*, vol. 13, no. 4, pp. 471–494, October 1966.

[82] J. C. Russ, *The Image Processing Handbook*, 3rd ed. Boca Raton, Florida: CRC Press LLC, 1999.

[83] P. K. Sahoo, S. Soltani, A. K. C. Wong, and Y. C. Chen, "A survey of thresholding techniques," *Computer Vision, Graphics, and Image Processing*, vol. 41, no. 2, pp. 233–260, February 1988.

[84] T. L. Saito, M. Ohtani, H. Sawai, F. Sano, A. Saka, D. Watanabe, M. Yukawa, Y. Ohya, and S. Morishita, "SCMD: *Saccharomyces cerevisiae* morphological database," *Nucleic Acids Research*, vol. 32, pp. D319–D322, January 2004.

[85] H. Sato, T. Takino, Y. Okada, J. Cao, A. Shinagawa, E. Yamamoto, and M. Seiki, "A matrix metalloproteinase expressed on the surface of invasive tumour cells," *Nature*, vol. 370, no. 6484, pp. 61–65, July 1994.

[86] M. P. Schönermark, O. Bock, A. Büchner, R. Steinmeier, U. Benbow, and T. Lenarz, "Quantification of tumor cell invasion using confocal laser scan microscopy," *Nature Medicine*, vol. 3, no. 10, pp. 1167–1171, October 1997.

[87] J. Selinummi, J.-R. Sarkanen, A. Niemistö, M.-L. Linne, T. Ylikomi, O. Yli-Harja, and T. O. Jalonen, "Quantification of vesicles in differentiating human SH-SY5Y neuroblastoma cells by automated image analysis," *Neuroscience Letters*, vol. 396, no. 2, pp. 102–107, March 2006.

[88] J. Serra, *Image Analysis and Mathematical Morphology*. London, England: Academic Press, 1982.

[89] M. Sezgin and B. Sankur, "Survey over image thresholding techniques and quantitative performance evaluation," *Journal of Electronic Imaging*, vol. 13, no. 1, pp. 146–165, January 2004.

[90] F. Y. Shih and W.-T. Wong, "Fully parallel thinning with tolerance to boundary noise," *Pattern Recognition*, vol. 27, no. 12, pp. 1677–1695, December 1994.

[91] M. E. Sieracki, S. E. Reichenbach, and K. L. Webb, "Evaluation of automated threshold selection methods for accurately sizing microscopic fluorescent cells by image analysis," *Applied and Environmental Microbiology*, vol. 55, no. 11, pp. 2762–2772, November 1989.

[92] R. Skipper and D. B. DeStephano, "A rapid stain for Campylobacter pylori in gastrointestinal sections using Diff-Quik," *Journal of Histotechnology*, vol. 12, no. 4, pp. 303–304, December 1989.

[93] P. Soille, *Morphological Image Analysis: Principles and Applications*, 2nd ed. Heidelberg, Germany: Springer Verlag, 2003.

[94] D. J. Stephens and V. J. Allan, "Light microscopy techniques for live cell imaging," *Science*, vol. 300, no. 5616, pp. 82–86, April 2003.

[95] G. Suzuki, H. Sawai, M. Ohtani, S. Nogami, F. Sano-Kumagai, A. Saka, M. Yukawa, T. L. Saito, J. Sese, D. Hirata, S. Morishita, and Y. Ohya., "Evaluation of image processing programs for accurate measurement of budding and fission yeast morphology," *Current Genetics*, vol. 49, no. 4, pp. 237–247, April 2006.

[96] E. W. Thompson, S. Nakamura, T. B. Shima, A. Melchiori, G. R. Martin, S. Z. Salahuddin, R. C. Gallo, and A. Albini, "Supernatants of acquired immunodeficiency syndrome-related Kaposi's sarcoma cells induce endothelial cell chemotaxis and invasiveness." *Cancer Research*, vol. 51, no. 10, pp. 2670–2676, May 1991.

[97] Y. A. Tolias and S. M. Panas, "A fuzzy vessel tracking algorithm for retinal images based on fuzzy clustering," *IEEE Transactions on Medical Imaging*, vol. 17, no. 2, pp. 263–273, April 1998.

[98] D. Tomazevic, B. Likar, and F. Pernus, "A comparison of retrospective shading correction techniques," in *Proceedings of the 15th International Conference on Pattern Recognition (ICPR'00)*, vol. 3, Barcelona, Spain, September 3–8, 2000, pp. 564–567.

[99] L. J. van Vliet, F. R. Boddeke, D. Sudar, and I. T. Young, "Image detectors for digital image microscopy," in *Digital Image Analysis of Microbes: Imaging, Morphometry, Fluorometry and Motility Techniques and Applications*, M. H. F. Wilkinson and F. Schut, Eds. Chichester, England: Wiley, 1998, pp. 37–64.

[100] D. Webb, M. A. Hamilton, G. J. Harkin, S. Lawrence, A. K. Camper, and Z. Lewandowski, "Assessing technician effects when extracting quantities from microscope images," *Journal of Microbiological Methods*, vol. 53, no. 1, pp. 97–106, April 2003.

[101] D. B. Wheeler, A. E. Carpenter, and D. M. Sabatini, "Cell microarrays and RNA interference chip away at gene function," *Nature Genetics*, vol. 37, no. Supplement 1, pp. S25–S30, June 2005.

[102] R. Wild, S. Ramakrishnan, J. Sedgewick, and A. W. Griffioen, "Quantitative assessment of angiogenesis and tumor vessel architecture by computer-assisted digital image analysis: effects of VEGF-toxin conjugate on tumor microvessel density," *Microvascular Research*, vol. 59, no. 3, pp. 368–376, May 2000.

[103] D. Wilkinson and J. F. Willemsen, "Invasion percolation: a new form of percolation theory," *Journal of Physics A: Mathematical and General*, vol. 16, no. 14, pp. 3365–3376, October 1983.

[104] M. Wirth, M. Fraschini, M. Masek, M. Bruynooghe, and M. Moonen, Eds., *EURASIP Journal on Applied Signal Processing: Special Issue on Performance Evaluation in Image Processing*, 2006.

[105] T. A. Witten and L. M. Sander, "Diffusion-limited aggregation, a kinetic critical phenomenon," *Physical Review Letters*, vol. 47, no. 19, pp. 1400–1403, November 1981.

[106] G. W. Wyszecki and S. W. Stiles, *Color Science: Concepts and Methods, Quantitative Data and Formulas*. New York: Wiley, 1982.

[107] C. Wählby, J. Lindblad, E. B. Mikael Vondrus, and L. Björkesten, "Algorithms for cytoplasm segmentation of fluorescence labeled cells," *Analytical Cellular Pathology*, vol. 24, no. 2–3, pp. 101–111, 2002.

[108] C. Wählby, I.-M. Sintorn, P. Erlandson, G. Borgefors, and E. Bengtsson, "Combining intensity, edge, and shape information for 2D and 3D segmentation of cell nuclei in tissue sections," *Journal of Microscopy*, vol. 215, no. 1, pp. 67–76, July 2004.

[109] A. Zaniboni and R. Labianca, "Adjuvant therapy for stage II colon cancer: an elephant in the living room?" *Annals of oncology*, vol. 15, no. 9, pp. 1310–1318, September 2004.

[110] J. Ziauddin and D. M. Sabatini, "Microarrays of cells expressing defined cDNAs," *Nature*, vol. 411, no. 6833, pp. 107–110, May 2001.

Publications

Publication I

A. Niemistö, V. Dunmire, O. Yli-Harja, W. Zhang, and I. Shmulevich, “Robust quantification of *in vitro* angiogenesis through image analysis,” *IEEE Transactions on Medical Imaging*, vol. 24, no. 4, pp. 549–553, April 2005.

Publication II

A. Niemistö, V. Dunmire, O. Yli-Harja, W. Zhang, and I. Shmulevich, “Analysis of angiogenesis using *in vitro* experiments and stochastic growth models,” *Physical Review E*, vol. 72, no. 6, 062902(1–4), December 2005.

Publication III

A. Niemistö, L. Hu, O. Yli-Harja, W. Zhang, and I. Shmulevich, "Quantification of *in vitro* cell invasion through image analysis," in *Proceedings of the 26th Annual International Conference of the IEEE Engineering in Medicine and Biology Society (EMBC'04)*, San Francisco, California, USA, September 1–5, 2004, pp. 1703–1706.

Publication IV

A. Niemistö, T. Aho, H. Thesleff, M. Tiainen, K. Marjanen, M.-L. Linne, and O. Yli-Harja, “Estimation of population effects in synchronized budding yeast experiments,” in *Image Processing: Algorithms and Systems II*, E. R. Dougherty, J. Astola, and K. Egiazarian, Eds. Proceedings of SPIE, vol. 5014, May 2003, pp. 448–459.

Publication V

A. Niemistö, J. Selinummi, R. Saleem, I. Shmulevich, J. Aitchison, and O. Yli-Harja, "Extraction of the number of peroxisomes in yeast cells by automated image analysis," in *Proceedings of the 28th Annual International Conference of the IEEE Engineering in Medicine and Biology Society (EMBC'06)*, New York, USA, August 30 – September 3, 2006, pp. 2353–2356.

Publication VI

A. Niemistö, I. Shmulevich, O. Yli-Harja, L. Chirieac, S. R. Hamilton, “Automated Quantification of Lymph Node Size and Number in Surgical Specimens of Stage II Colorectal Cancer,” in *Proceedings of the 27th Annual International Conference of the IEEE Engineering in Medicine and Biology Society (EMBC’05)*, Shanghai, China, September 1–4, 2005, pp. 6313-6316.

Publication VII

A. Niemistö, I. Shmulevich, V. Lukin, A. Dolia, and O. Yli-Harja, “Correction of misclassifications using a proximity-based estimation method,” *EURASIP Journal on Applied Signal Processing*, vol. 2004, no. 8, pp. 1142–1155, August 2004.

Tampereen teknillinen yliopisto
PL 527
33101 Tampere

Tampere University of Technology
P.O. Box 527
FIN-33101 Tampere, Finland